Mon. Not. R. Astron. Soc. **000**, 000–000 (0000) Printed 5 September 2008 (MN LATEX style file v1.4)

The Aquarius Project: the subhalos of galactic halos

V. Springel[1], J. Wang[1], M. Vogelsberger[1], A. Ludlow[2], A. Jenkins[3], A. Helmi[4], J. F. Navarro[2,5], C. S. Frenk[3], and S. D. M. White[1]

[1] *Max-Planck-Institut für Astrophysik, Karl-Schwarzschild-Straße 1, 85740 Garching bei München, Germany*
[2] *Dep. of Physics & Astron., University of Victoria, Victoria, BC, V8P 5C2, Canada*
[3] *Institute for Computational Cosmology, Dep. of Physics, Univ. of Durham, South Road, Durham DH1 3LE, UK*
[4] *Kapteyn Astronomical Institute, Univ. of Groningen, P.O. Box 800, 9700 AV Groningen, The Netherlands*
[5] *Department of Astronomy, University of Massachusetts, Amherst, MA 01003-9305, USA*

5 September 2008

ABSTRACT

We have performed the largest ever particle simulation of a Milky Way-sized dark matter halo, and present the most comprehensive convergence study for an individual dark matter halo carried out thus far. We have also simulated a *sample* of 6 ultra-highly resolved Milky-way sized halos, allowing us to estimate the halo-to-halo scatter in substructure statistics. In our largest simulation, we resolve nearly 300,000 gravitationally bound subhalos within the virialized region of the halo. Simulations of the same object differing in mass resolution by factors up to 1800 accurately reproduce the largest subhalos with the same mass, maximum circular velocity and position, and yield good convergence for the abundance and internal properties of dark matter substructures. We detect up to four generations of subhalos within subhalos, but contrary to recent claims, we find less substructure in subhalos than in the main halo when regions of equal mean overdensity are compared. The overall substructure mass fraction is much lower in subhalos than in the main halo. Extrapolating the main halo's subhalo mass spectrum down to an Earth mass, we predict the mass fraction in substructure to be well below 3% within 100 kpc, and to be below 0.1% within the Solar Circle. The inner density profiles of subhalos show no sign of converging to a fixed asymptotic slope and are well fit by gently curving profiles of Einasto form. The mean concentrations of isolated halos are accurately described by the fitting formula of Neto et al. down to maximum circular velocities of $1.5\,\mathrm{km\,s^{-1}}$, an extrapolation over some 5 orders of magnitude in mass. However, at equal maximum circular velocity, subhalos are more concentrated than field halos, with a characteristic density that is typically ~ 2.6 times larger and increases with decreasing distance from halo centre.

Key words: cosmology: dark matter – methods: numerical

1 INTRODUCTION

A major puzzle in Cosmology is that the main matter component in today's Universe appears to be in the form of a yet-undiscovered elementary particle whose contribution to the cosmic density is more than 5 times that of ordinary baryonic matter (e.g. Komatsu et al., 2008). This particle interacts extremely weakly with atoms and photons, so that gravity alone has affected its distribution since very early times. Recent observations have established a standard paradigm in which dark matter emerged from the early Universe with negligible thermal velocities and a gaussian and scale-free distribution of density fluctuations. In this "Cold Dark Matter" (CDM) hypothesis, quantum fluctuations during a very early period of cosmic inflation determine the statistics of the dark matter distribution at early epochs when the Universe was almost uniform (Guth, 1981; Starobinsky, 1982; Hawking, 1982; Bardeen et al., 1983). Galaxies form from these initial conditions through the condensation of gas at the centres of a hierarchically aggregating population of quasi-equilibrium dark matter halos (White & Rees, 1978; White & Frenk, 1991).

When the effects of the baryons can be neglected, the nonlinear growth of dark matter structure is a well-posed problem where both the initial conditions and the evolution equations are known. This is an N-body problem *par*

⋆ E-mail: volker@mpa-garching.mpg.de

excellence. The faithfulness of late-time predictions (which must be confronted directly with observation to test the paradigm) is limited purely by numerical technique and by the available computing resources.

Over the past two decades, numerical simulations have played a pivotal role in establishing the viability of the CDM paradigm (e.g. Davis et al., 1985; Frenk et al., 1988; Warren et al., 1992; Gelb & Bertschinger, 1994; Cen et al., 1994; Hernquist et al., 1996; Jenkins et al., 2001; Wambsganss et al., 2004). They have led to the discovery of a universal internal structure for dark matter halos (Navarro et al., 1996, 1997, hereafter NFW), and they have supplied precise predictions for the expected large-scale structure of the Universe. The matter distribution on scales from ~ 50 kpc to the size of the observable Universe and the galaxy population predicted by hierarchical CDM scenarios have been compared directly with a wide array of observations. A recent example is the "Millennium Run" (Springel et al., 2005), still one of the largest cosmological simulations ever carried out, which followed the formation and evolution of over 10 million galaxies by post-processing the stored simulation outputs (Croton et al., 2006; Bower et al., 2006). So far, the ΛCDM paradigm has passed these tests successfully, particularly those that consider the large-scale matter distribution.

Given this success in reproducing the large-scale structure of the Universe, it is important to test CDM predictions also on smaller scales, not least because these are sensitive to the nature of the dark matter. Indeed, a number of serious challenges to the paradigm have emerged on the scale of individual galaxies and their central structure. The realisation that CDM halos have cuspy dark matter density profiles led to a fierce debate about whether these are consistent with the rotation curves observed for low surface brightness, apparently dark matter dominated galaxies (Flores & Primack, 1994; Moore, 1994; McGaugh & de Blok, 1998; de Blok et al., 2001; Hayashi et al., 2004; Hayashi & Navarro, 2006). The abundance of small dark matter subhalos predicted within CDM halos has also drawn much attention (Klypin et al., 1999; Moore et al., 1999a). The total number is much larger than the number of known satellite galaxies surrounding the Milky Way, even accounting for the many recently discovered faint systems. It is still unclear whether this reflects an absence of the predicted low mass objects or merely the fact that no stars were able to form within them. The issue of dark matter substructure within halos is made more urgent by the prospect of observing dark matter particles in the near future, either by their annihilation radiation (e.g. Bergström et al., 1998), or through direct detection in experiments here on Earth (reviewed, e.g., by Gaitskell, 2004). For both, a precise and quantitative understanding of the small-scale dark matter distribution within our Galaxy is needed.

Our Aquarius Project addresses these questions by studying the highly nonlinear structure of Galaxy-sized CDM halos in unprecedented detail using state-of-the art numerical simulations. We are particularly interested in the inner regions of these halos and of their substructures, where the density contrast exceeds 10^6 and the astrophysical consequences of the nature of dark matter may be most clearly apparent. Quantifying such structure reliably through simulation is an acute challenge to numerical technique. In order to address this challenge, we use a newly developed version of our parallel simulation code, GADGET-3 (based on Springel et al., 2001b; Springel, 2005), which allows us to cover an unprecedented dynamic range at high numerical accuracy. We carefully validate our simulation techniques and establish their range of numerical convergence through systematic convergence studies, thereby building confidence in the reliability of our results.

In order to evaluate the scatter in structural properties between halos, we have simulated six different systems at high resolution, each having between 160 and 224 million particles within r_{50}, the radius with mean enclosed overdensity 50 times the critical value.* Each of these simulations is better resolved than any previously published high-resolution halo simulation except the very recent 'Via Lactea II' run of Diemand et al. (2008) which has 470 million particles within r_{50}. For one of our halos, we have increased the resolution by a further factor of 8, pushing the particle number within r_{50} to 1.47 billion. The gravitational softening length of this largest run is just 20.5 pc. We collectively refer to this suite of simulations as the Aquarius Project.

In the present paper, we describe our simulation techniques and analyze a number of basic properties of our $z = 0$ halos. We focus in particular on the abundance of substructures, their radial distribution, and their internal density profiles. We also give results for the concentration of substructures, and for the fraction of the mass they contain at different radii. In a companion paper (Springel et al., 2008), we study implications for the detectability of dark matter annihilation within the Milky Way's dark matter halo, and in Navarro et al. (2008) we study the structure of the central density cusps of the main halos. Future papers will study the evolution of our halos and their substructure.

This paper is organized as follows. In Section 2, we introduce our simulation set and describe our numerical techniques. The abundance of dark matter substructures and their radial distribution within our halos are analyzed in Section 3. Then, in Section 4, we turn to an analysis of the abundance of substructure within subhalos. In Section 5, we consider the density profiles of subhalos and their concentrations. Finally, we summarize our conclusions in Section 6.

2 SIMULATION SET AND NUMERICAL TECHNIQUES

All our simulations follow halo formation within a periodic cube of side $100\,h^{-1}\mathrm{Mpc} \simeq 137\,\mathrm{Mpc}$ in a cosmology with parameters $\Omega_m = 0.25$, $\Omega_\Lambda = 0.75$, $\sigma_8 = 0.9$, $n_s = 1$, and Hubble constant $H_0 = 100\,h\,\mathrm{km\,s^{-1}\,Mpc^{-1}} = 73\,\mathrm{km\,s^{-1}\,Mpc^{-1}}$. These cosmological parameters are the same as used in the Millennium Simulation project, and are consistent with the current set of cosmological constraints within their uncertainties, in particular those from the WMAP 1- and 5-year data analyses.

* We use this unconventional outer radius for our halos, rather than the standard r_{200}, to facilitate comparison with Diemand et al. (2007a, 2008) who quote results for their Via Lactea simulations within r_{50} although they refer to this radius as "r_{200}".

Name	$m_{\rm p}$ [$M_\odot$]	ϵ [pc]	$N_{\rm hr}$	$N_{\rm lr}$	M_{200} [$M_\odot$]	r_{200} [kpc]	M_{50} [$M_\odot$]	r_{50} [kpc]	N_{50}
Aq-A-1	1.712×10^3	20.5	4,252,607,000	144,979,154	1.839×10^{12}	245.76	2.523×10^{12}	433.48	1,473,568,512
Aq-A-2	1.370×10^4	65.8	531,570,000	75,296,170	1.842×10^{12}	245.88	2.524×10^{12}	433.52	184,243,536
Aq-A-3	4.911×10^4	120.5	148,285,000	20,035,279	1.836×10^{12}	245.64	2.524×10^{12}	433.50	51,391,468
Aq-A-4	3.929×10^5	342.5	18,535,972	634,793	1.838×10^{12}	245.70	2.524×10^{12}	433.52	6,424,399
Aq-A-5	3.143×10^6	684.9	2,316,893	634,793	1.853×10^{12}	246.37	2.541×10^{12}	434.50	808,479
Aq-B-2	6.447×10^3	65.8	658,815,010	80,487,598	8.194×10^{11}	187.70	1.045×10^{12}	323.12	162,084,992
Aq-B-4	2.242×10^5	342.5	18,949,101	648,874	8.345×10^{11}	188.85	1.050×10^{12}	323.60	4,683,037
Aq-C-2	1.399×10^4	65.8	612,602,795	78,634,854	1.774×10^{12}	242.82	2.248×10^{12}	417.09	160,630,624
Aq-C-4	3.213×10^5	342.5	26,679,146	613,141	1.793×10^{12}	243.68	2.285×10^{12}	419.36	7,110,775
Aq-D-2	1.397×10^4	65.8	391,881,102	79,615,274	1.774×10^{12}	242.85	2.519×10^{12}	433.21	180,230,512
Aq-D-4	2.677×10^5	342.4	20,455,156	625,272	1.791×10^{12}	243.60	2.565×10^{12}	435.85	9,579,672
Aq-E-2	9.593×10^3	65.8	465,905,916	74,119,996	1.185×10^{12}	212.28	1.548×10^{12}	368.30	161,323,676
Aq-E-4	2.604×10^5	342.5	17,159,996	633,106	1.208×10^{12}	213.63	1.558×10^{12}	369.14	5,982,797
Aq-F-2	6.776×10^3	65.8	414,336,000	712,839	1.135×10^{12}	209.21	1.517×10^{12}	365.87	223,901,216
Aq-F-3	2.287×10^4	120.5	122,766,400	712,839	1.101×10^{12}	207.15	1.494×10^{12}	363.98	65,320,572

Table 1. Basic parameters of the Aquarius simulations. We have simulated 6 different halos, each at several different numerical resolutions. The leftmost column gives the simulation name, encoding the halo (A to F), and the resolution level (1 to 5). $m_{\rm p}$ is the particle mass, ϵ is the Plummer equivalent gravitational softening length, $N_{\rm hr}$ is the number of high resolution particles, and $N_{\rm lr}$ the number of low resolution particles filling the rest of the volume. M_{200} is the virial mass of the halo, defined as the mass enclosed in a sphere with mean density 200 times the critical value. r_{200} gives the corresponding virial radius. We also give the mass and radius for a sphere of overdensity 50 times the critical density, denoted as M_{50} and r_{50}. Note that this radius encloses a mean density 200 times the *background density*; in some studies (e.g. Diemand et al., 2007a) M_{50} and r_{50} have been defined as virial mass and radius. Finally, N_{50} gives the number of simulation particles within r_{50}.

2.1 Setting the initial conditions

The linear power spectrum used for making the initial conditions is based on a transfer function made by CMBFAST (v4.5.1, Seljak & Zaldarriaga, 1996) with $\Omega_{\rm baryon} = 0.045$. The transfer function was evaluated at $z = 0$ where the CDM and baryon transfer functions are virtually identical for wavenumbers k up to $\log_{10}(kh/{\rm Mpc}) = 2.5$. For higher wavenumbers the effects of pressure are important for the baryons and are reflected in a feature present also in the CDM transfer function. Given that our simulations model only a CDM component and cannot account for the separate evolution of the baryons, we have chosen to ignore this baryon induced feature for our CDM power spectrum and have instead created a smooth composite transfer function (explained in detail below) which lacks this feature. In practice, for the Aquarius simulations, the difference between using our composite transfer function and the CMBFAST transfer function is relatively modest. The size of the difference can be gauged by considering the fractional change in the *rms* linear density fluctuations for a spherical top-hat filter enclosing a mass of mean density corresponding to 32 particles (our resolution limit in the subsequent analyses). For our highest resolution simulation the *rms* using our composite transfer function is less than 2% above that using the CMBFAST CDM transfer function. For all other simulations the difference is even smaller.

Our composite transfer function was formed as follows. It was set equal to the CMBFAST transfer function for $\log_{10}(kh/{\rm Mpc}) < 1$, and equal to an analytic form based on the CDM only transfer function of Bardeen et al. (1986, hereafter BBKS) for $\log_{10}(kh/{\rm Mpc}) > 2$. Over the intermediate range the composite transfer function is given by the linear combination of $(1 - w)$ times the CMBFAST and w times the BBKS transfer function, where the weighting function w changes smoothly from 0 to 1. By using a value of $\Gamma = 0.16$ for the shape parameter in the BBKS formula and scaling the overall amplitude it proved possible to match the amplitudes of the CMBFAST and BBKS functions everywhere in the transition region, $1 < \log_{10}(kh/{\rm Mpc}) < 2$, to better than 0.5%, with the result that the overall transfer function is very smooth.

We selected target halos for resimulation from a parent simulation carried out at homogeneous resolution with 900^3 particles in this same box. We targeted halos of roughly Milky Way mass and without a massive close neighbour at $z = 0$. We also checked that semi-analytic modelling applied to our target halos predicated them to host late-type galaxies. Otherwise our selection was random. New initial conditions for the selected objects were then constructed by identifying the Lagrangian region from which each halo formed. The high resolution region, which has an 'amoeba'-like shape, was defined as the union of a set of small identical cubes joined face to face covering the whole of the Lagrangian region and forming a simply connected volume. Within this region the mass distribution was represented by a much larger number of lower mass particles. On making the initial conditions, additional small-scale power was added to the high resolution region as dictated by the higher local particle Nyquist frequency. More distant regions were sampled with progressively more massive particles, but retaining sufficient resolution to ensure an accurate representation of the tidal field at all times. The initial displacements were imprinted using the Zeldovich approximation,

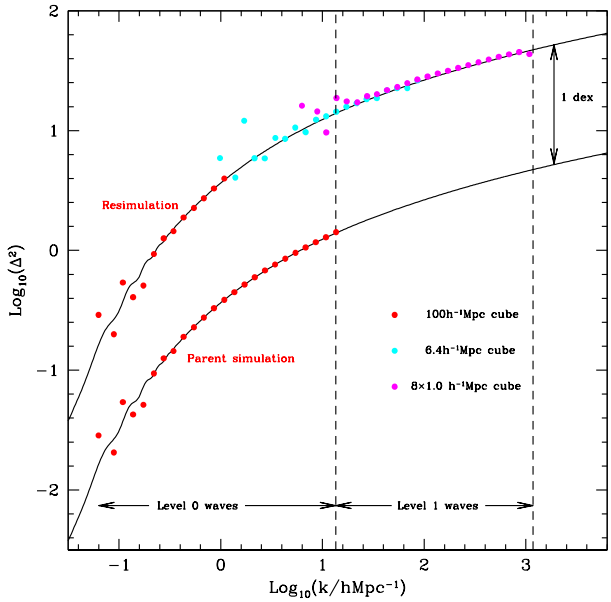

Figure 1. Measured power spectrum (dimensionless variance $\Delta^2(k) \sim k^3 P(k)$ per natural log interval) in our highest resolution 'zoom' initial conditions, Aq-A-1, linearly extrapolated to the values expected at $z = 0$. The lower red points show the power spectrum measured in our homogeneously sampled parent simulation, shifted down by one dex for clarity. The upper red circles show our measurement for the zoom initial conditions for the whole box, while cyan and magenta circles show measurements from smaller boxes centred within the high-resolution region. The solid black lines show the linear theory input spectrum. The vertical dashed line on the right marks the Nyquist frequency of the high-resolution region, while the left vertical line is the joining point between the long wavelength modes from the parent simulation and the high frequency modes added to the high resolution cube.

and a 'glass-like' uniform particle load (White, 1996) was used within the high-resolution regions of all our initial conditions. We also invested particular care to guarantee that all our final halos are unaffected by contamination by heavier boundary particles. In fact, all our halos are free of *any* boundary particles within the radius r_{50}, except for simulations Aq-E-2, Aq-F-2, and Aq-F-3, where 71, 9, and 3 heavier particles are found within this radius, respectively, corresponding to a fraction $\lesssim 10^{-5}$ of the total mass within this radius. Typically, about 30% of the high-resolution particles in the new initial conditions end up in the virialized region of the final halo.

In setting up these zoomed initial conditions, all power from the parent simulation is deleted beyond some wavenumber which is smaller than the Nyquist wavenumber of the parent simulation, but substantially larger than the fundamental wavenumber of the cube enclosing the high resolution region in which we generate the additional high frequency waves. The latter replace the waves deleted from the fluctuation field of the parent simulation and extend its power spectrum up to the Nyquist frequency corresponding to the mean interparticle separation in the high-resolution region. When we create a series of simulations of the same object at differing mass resolution (i.e. with different particle masses in the high resolution region) we are careful to ensure that all the waves used to create a lower resolution simulation are present with identical amplitude and phase in all higher resolution simulations. This means that every object which forms in the lower resolution simulation should also be present with identical mass and position in its higher resolution counterparts. This allows us to make detailed convergence tests on the properties of every nonlinear object in our simulations, not just on the main halo.

In Figure 1, we show the power spectrum as measured from the initial conditions of our highest resolution resimulation, Aq-A-1 from Table 1. All the measurements are made using a 1000^3 Fourier transform using a cloud-in-cell assignment scheme and taking into account for each mode the expected smoothing effect of the assignment scheme. Measuring the power spectrum accurately however requires a further measure. Even in the absence of the imposed perturbations, the unperturbed particle distribution has some measurable power. This power in a discrete particle representation, unlike a truely uniform mass distribution, does not grow by gravitational instability. Over most scales this extra power is negligible compared to that introduced when the density perturbations are added by displacing the particles which we wish to measure. However at scales approaching the particle Nyquist frequency the contribution from the unperturbed particle distribution starts to become significant compared to the imposed power. To allow for this effect, which would otherwise lead to an overestimate of the input power, the values for all the points plotted are computed by differencing the power of the perturbed and unperturbed particle positions.

In Figure 1 the lower sequence of red filled circles shows the measured power spectrum (linearly extrapolated to $z = 0$ and offset by exactly one dex for clarity) from the parent 900^3 particle simulation, plotted down to the shortest wavelength included in the refined initial conditions. The two black curves show the theoretical linear power spectrum, discussed above, with the upper curve extrapolated to $z = 0$ and the lower curve shifted down from it by one dex. The power spectrum of the parent simulation is evidently a very good match to the theoretical power spectrum except at low k where close agreement is not expected because only a few modes contribute. The upper red circles show the power spectrum measured in the initial conditions of the zoom simulation (linearly extrapolated to $z = 0$). The most massive particles in the refined initial conditions have a mass $1/41^3$ of the entire $100\,h^{-1}$Mpc box. As the Nyquist frequency for particles of this mass corresponds to $\log(k\,h\,\mathrm{Mpc}^{-1}) = 0.11$, only points to the left of this limit are plotted. The cyan circles show the power spectrum measured from a box of side length $6.4\,h^{-1}$Mpc centred on the high resolution region. The masses of the particles in this region vary, with the most massive particles having a mass of $\sim 7.23 \times 10^{-8}$ of the region within which high-frequency power is added. (The latter is cubic with a side length of $7.06\,h^{-1}$Mpc.) The Nyquist frequency corresponding to the most massive particles is here $\log(k\,h\,\mathrm{Mpc}^{-1}) = 2.03$, and the cyan points are shown only to the left of this limit.

Finally, the magenta circles show the average power spectrum measured from eight boxes of side-length $1\,h^{-1}$Mpc inside the central high resolution region, where

all the particles are of the same mass. The largest possible cube that can be extracted where all the particles have the same mass is about $2.4\,h^{-1}$Mpc on a side. A 1000^3 Fourier transform is not large enough to make an accurate measurement of the power spectrum over this size of cube because the particle and Fourier mesh Nyquist frequencies are very close. Instead we placed 8 non-overlapping $1\,h^{-1}$Mpc cubes inside this volume. Averaging the eight regions reduces the expected scatter at low wavenumber, but makes no significant difference compared to a single measurement at high wave-numbers. Again the points are only plotted up to their Nyquist frequency, which is marked by the rightmost vertical dashed line. The leftmost vertical dashed line marks the joining point in the high-resolution cube between the long-wavelength waves from the parent simulation and the high-frequency waves in the high-resolution cube. The joining point corresponds to about 15 waves across the high-resolution cube.

These measurements of the power spectrum of our initial conditions show that we clearly achieve an excellent match to the desired linear input spectrum over many decades in spatial scale. We stress that such tests of the initial conditions are essential, as their quality is obviously of paramount importance for the accuracy of the evolved simulations. Note that in the following, "high-resolution region" refers to the amoeba-shaped region where all the particles have the same mass rather than to the region to which high frequency waves are added (which is larger). Similarly, the low-resolution region is everything outside the amoeba.

2.2 The Aquarius simulation suite

In Table 1, we provide an overview of the basic numerical parameters of our simulations. This includes a symbolic simulation name, the particle mass in the high-resolution region, the gravitational softening length, the total particle numbers in the high- and low-resolution regions, as well as various characteristic masses and radii for the final halos, and the corresponding particle numbers. Our naming convention is such that we use the tags "Aq-A" to "Aq-F" to refer to simulations of the six Aquarius halos. An additional suffix "1" to "5" denotes the resolution level. "Aq-A-1" is our highest resolution calculation with ~ 1.5 billion halo particles. We have level 2 simulations of all 6 halos, corresponding to 160 to 224 million particles per halo.

We kept the gravitational softening length fixed in comoving coordinates throughout the evolution of all our halos. The dynamics is then governed by a Hamiltonian and the phase-space density of the discretized particle system should be strictly conserved as a function of time (Springel, 2005), modulo the noise introduced by finite force and time integration errors. Timestepping was carried out with a kick-drift-kick leap-frog integrator where the timesteps were based on the local gravitational acceleration, together with a conservatively chosen maximum allowed timestep for all particles.

We define the virial mass M_Δ and viral radius r_Δ as the mass and radius of a sphere that encloses a mean density $\Delta \times \rho_{\rm crit}$, where $\rho_{\rm crit}$ is the critical density. Different choices for Δ are used in the literature. The most common ones are (1) a fixed value of $\Delta = 200$ as in NFW's original work, (2) a value of $\Delta \sim 178\,\Omega_m^{0.45}$ based on a generalization of the spherical top-hat collapse model to low density cosmologies (Eke et al., 1996; Bryan & Norman, 1998), or (3) a value of $\Delta = 200\,\Omega_m(z)$, which corresponds to a fixed overdensity relative to the background density.

We will frequently give results for the radius according to convention (3), for which $\Delta = 200\,\Omega_m = 50$ at $z = 0$, simply because this yields the largest radius and hence the largest number of substructures, which improves statistics. The corresponding radius is designated as r_{50}, while r_{200} refers to the radius that encloses an overdensity of 200 with respect to the critical density, as is customary in the literature (except for Diemand et al., 2007a, and collaborators, who use r_{200} to refer to a radius that encloses 200 times the *mean density*, which is equivalent to r_{50} in our notation).

2.3 Integration technique

All our simulations were started at redshift $z = 127$, and were evolved with a new parallel TreePM code GADGET-3 written especially for the Aquarius project. This code offers much better scalability to large numbers of compute cores as well as higher basic speed than its parent code GADGET-2 (Springel, 2005). The gravitational field on large scales is calculated with a particle-mesh (PM) algorithm, while the short-range forces are delivered by a tree-based hierarchical multipole expansion, such that a very accurate and fast gravitational solver results. The scheme combines the high spatial resolution and relative insensitivity to clustering of tree algorithms with the unmatched speed and accuracy of the PM method to calculate the long range gravitational field. We note that achieving our force resolution with a single mesh in a standard PM approach would require a grid with $(10^7)^3$ cells – storing such a mesh would require several million petabytes. This illustrates the enormous dynamic range we are aiming for with our simulations.

In fact, the numerical challenge of the calculations is substantial. One challenge simply reflects the large dynamic range involved: gravitational timescales are inversely proportional to the square root of the density, so simulating a CDM halo means dealing with a system where different regions evolve on timescales which may differ by factors of thousands. A code with spatially-dependent, adaptive timestepping is mandatory; otherwise the most rapidly evolving regions – which usually include only a tiny fraction of the mass – force timesteps so short that the calculation grinds to a halt. A second challenge stems from the highly clustered spatial distribution of matter and affects, in particular, the scalability of parallel algorithms. A CDM halo is a nearly monolithic, highly concentrated structure with a well-defined centre. There is no obvious geometrical decomposition which can separate it into the large number of computationally equivalent domains required for optimal exploitation of the many processors available in high-performance parallel architectures. In our highest resolution calculation, the clustering is so extreme that far more than a billion particles (amounting to about one third of all particles in the simulation) collect in a region that encompasses less than 10^{-8} of the simulated volume. In addition, gravity couples the dynamics of matter throughout the halo and beyond, requiring efficient communication between all parts of the simulated region.

It is clear that parallelization of such calculations for distributed memory machines is difficult, yet is mandatory

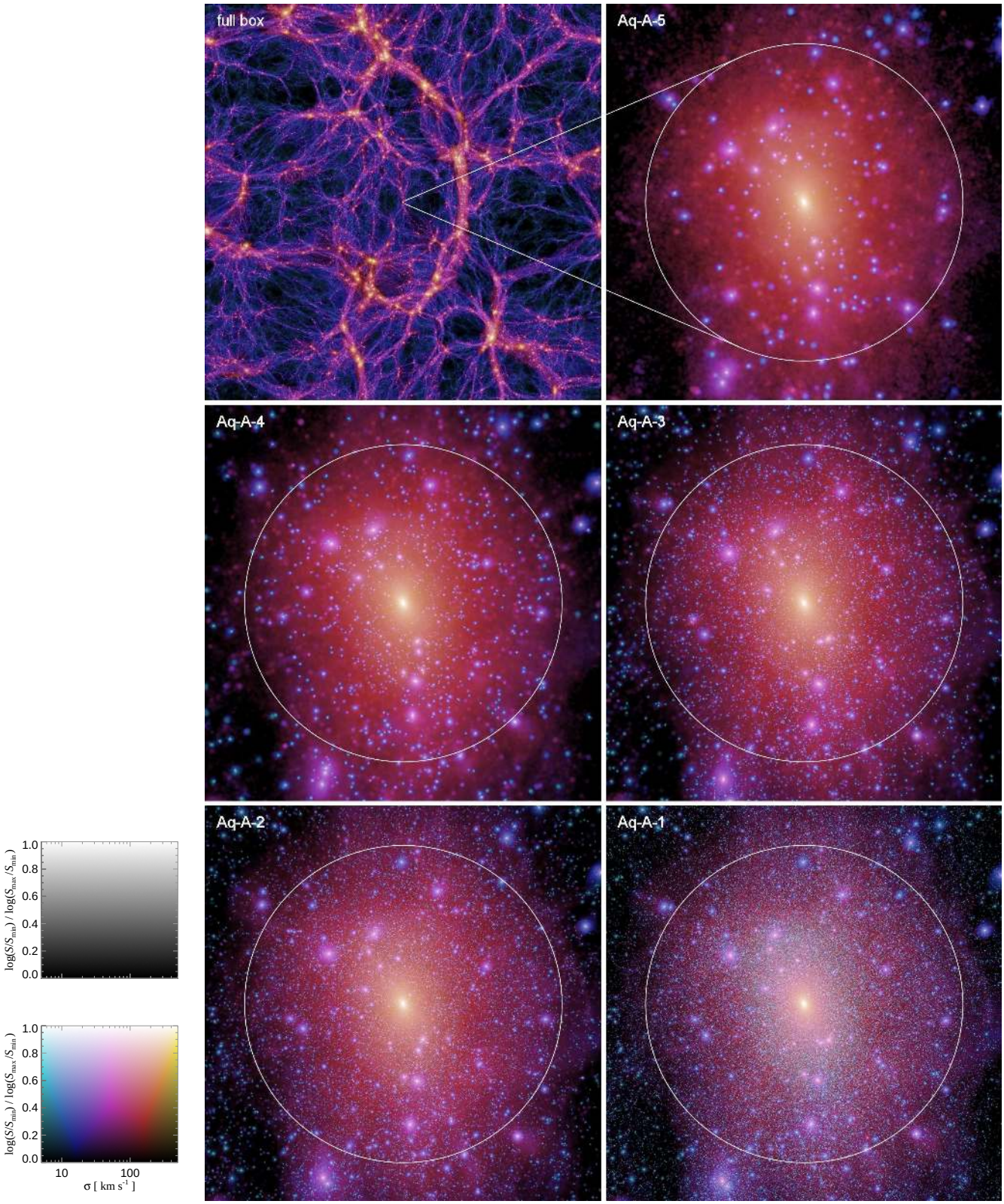

Figure 2. The top left panel shows the projected dark matter density at $z = 0$ in a slice of thickness 13.7 Mpc through the full box (137 Mpc on a side) of our 900^3 parent simulation, centred on the 'Aq-A' halo that was selected for resimulation. The other five panels show this halo resimulated at different numerical resolutions. In these panels, all particles within a cubic box of side-length $2.5 \times r_{50}$ centred on the halo are shown. The image brightness is proportional to the logarithm of the squared dark matter density $S(x, y)$ projected along the line-of-sight, and the colour hue encodes the local velocity dispersion weighted by the squared density along the line-of-sight. We use a two-dimensional colour table (as shown on the left) to show both of these quantities simultaneously. The colour hue information is orthogonal to the brightness information; when converted to black and white, only the density information remains, with a one-dimensional grey-scale colour map as shown on the left. The circles mark r_{50}.

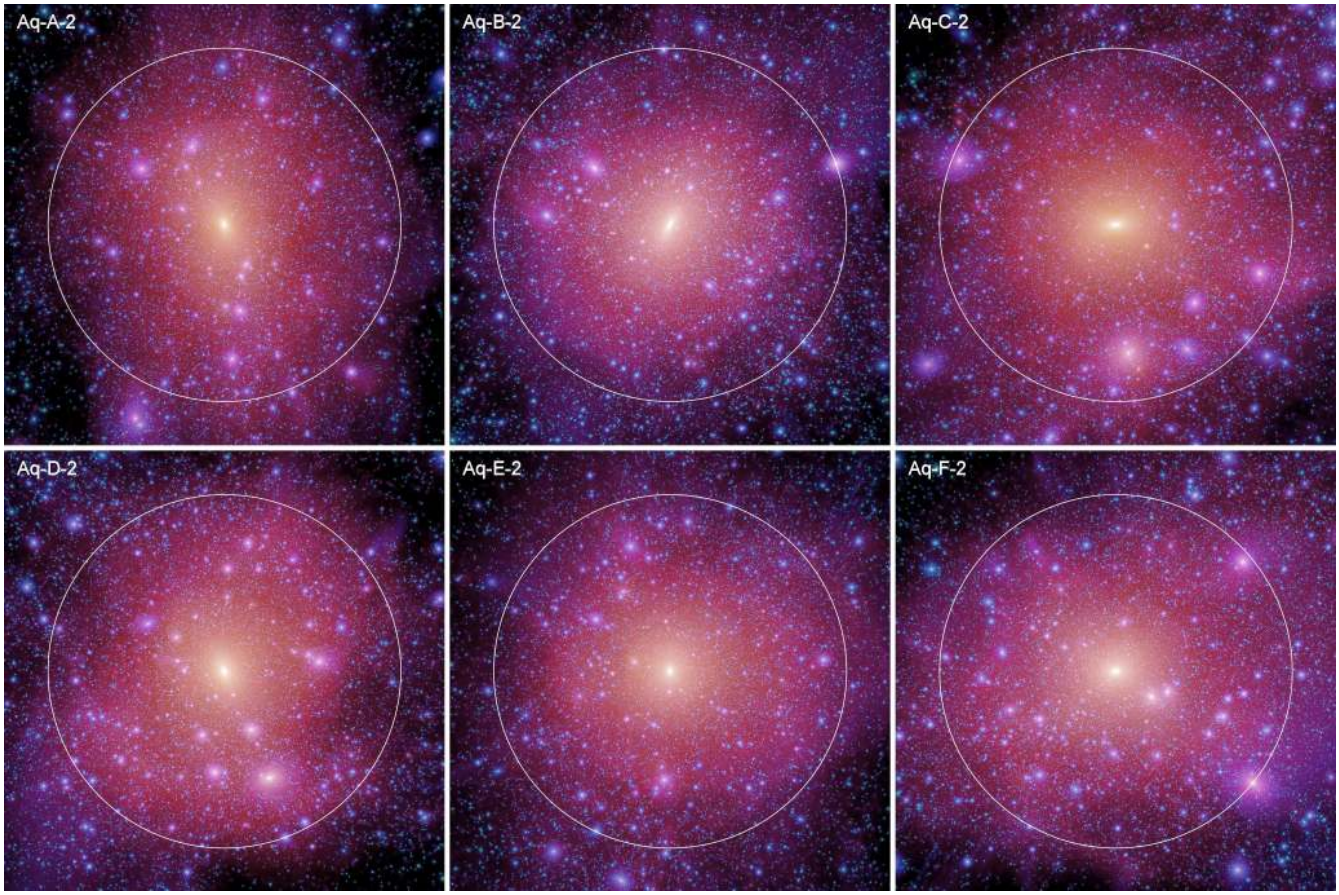

Figure 3. Projected dark matter density in our six different high-resolution halos at $z = 0$, at the '2' resolution level. In each panel, all particles within a cubic box of side length $2.5 \times r_{50}$ centred on the halo are shown, and the circles mark the radius r_{50}. The image brightness is proportional to the logarithm of the squared dark matter density, and the colour hue encodes the local particle velocity dispersion, with the same colour map as in Figure 2.

to make them feasible on today's supercomputers. We have carried out our most expensive calculation, the Aq-A-1 run, on the Altix 4700 supercomputer of the Leibniz Computing Center (LRZ) in Garching/Germany, using 1024 CPUs and about 3 TB of main memory. The calculation took more than 3.5 million CPU hours to carry out about 101400 timesteps that involved 6.72×10^{13} force calculations in total. We have stored 128 simulation dumps for this calculation, amounting to a data volume of about 45 TB. The other simulations of the Aquarius Project were in part calculated on the LRZ system, and in part on other supercomputers across Europe. These were the COSMA computer at Durham University/UK, the Bluegene/L system STELLA of the LOFAR consortium in Groningen/Netherlands, and a Bluegene/P system of the Max-Planck Computing Center in Garching. For all these simulations we also stored at least 128 outputs, but for Aq-A-2 and Aq-A-4 we kept 1024 dumps, and for Aq-A-3 half this number. This provides exquisite time resolution for studies of the detailed formation history of halos and the evolution of their substructure. In the present study, however, we focus on an analysis of the objects at $z = 0$.

2.4 A first view of the simulations

In Figures 2 and 3, we show images[†] of the dark matter distribution in our 6 high resolution halos at redshift $z = 0$. The brightness of each pixel is proportional to the logarithm of the squared dark matter density projected along the line-of-sight,

$$S(x, y) = \int \rho^2(\boldsymbol{r})\, \mathrm{d}z, \tag{1}$$

while the colour hue encodes the mean dark matter velocity dispersion, weighted as

$$\sigma(x, y) = \frac{1}{S(x, y)} \int \sigma_{\rm loc}(\boldsymbol{r})\, \rho^2(\boldsymbol{r})\, \mathrm{d}z. \tag{2}$$

Here the local dark matter density $\rho(\boldsymbol{r})$ and the local velocity dispersion $\sigma_{\rm loc}(\boldsymbol{r})$ of the particles are estimated with an SPH kernel interpolation scheme based on 64 neighbours. We use a two-dimensional colour-table (see Fig. 2) in which the information about the local dark matter 'temperature' is

[†] Further images and videos of the formation process of the halos are available at http://www.mpa-garching.mpg.de/aquarius

Name	$V_{\rm max}$ [km s^{-1}]	$r_{\rm max}$ [kpc]	δ_V	$c^*_{\rm NFW}$	$z_{\rm form}$	$N_{\rm sub}$	$f^{\rm cumul}_{\rm sub}$
Aq-A-1	208.75	28.35	2.035×10^4	16.11	1.93	297791	13.20 %
Aq-A-2	208.49	28.14	2.060×10^4	16.19	1.93	45024	12.16 %
Aq-A-3	209.22	27.88	2.114×10^4	16.35	1.93	13854	11.34 %
Aq-A-4	209.24	28.20	2.067×10^4	16.21	1.93	1960	9.68 %
Aq-A-5	209.17	28.55	2.015×10^4	16.04	1.93	299	8.64 %
Aq-B-2	157.68	40.15	5.788×10^3	9.72	1.39	42537	10.54 %
Aq-B-4	159.03	44.31	4.834×10^3	9.02	1.39	1614	8.26 %
Aq-C-2	222.40	32.47	1.761×10^4	15.21	2.23	35022	7.17 %
Aq-C-4	223.20	33.63	1.654×10^4	14.84	2.23	1972	6.02 %
Aq-D-2	203.20	54.08	5.299×10^3	9.37	1.51	47014	13.06 %
Aq-D-4	204.47	55.76	5.046×10^3	9.18	1.51	3116	10.67 %
Aq-E-2	179.00	55.50	3.904×10^3	8.26	2.26	42725	10.75 %
Aq-E-4	182.68	54.59	4.202×10^3	8.52	2.26	2024	7.53 %
Aq-F-2	169.08	42.67	5.892×10^3	9.79	0.55	52503	13.39 %
Aq-F-3	174.05	43.76	5.937×10^3	9.82	0.55	12950	9.15 %

Table 2. Basic structural properties of the main halos in our various simulations. The leftmost column gives the simulation name, $V_{\rm max}$ is the maximum circular velocity, $r_{\rm max}$ is the radius where this maximum is reached, δ_V gives the characteristic density contrast based on the peak of the circular velocity curve, while $c^\star_{\rm NFW}$ is the same value converted to an equivalent NFW concentration under the assumption that the halo is reasonably well fit by an NFW profile. $z_{\rm form}$ gives the formation redshift of the halo, defined as the earliest epoch at which the M_{200} mass of the main halo progenitor exceeds half its final value. Finally, $N_{\rm sub}$ gives the total number of subhalos that we resolve inside r_{50}, and $f^{\rm cumul}_{\rm sub}$ is their total mass fraction relative to all the mass inside r_{50}.

orthogonal to the density information; conversion of the images into grey-scale eliminates the velocity information but leaves the density information intact, with the latter being proportional to the dark matter annihilation luminosity.

Looking at these images it is clear that our halos are filled with a sea of dark matter substructures of many different sizes. Figure 2 shows that these repeat closely, as they should, between simulations of the same object at different resolution, albeit at slightly different positions. As we will show later in more detail, there are even substructures inside subhalos. In fact, up to four such generations are resolved by our highest resolution calculation, the Aq-A-1 version of the 'A' object. It is clear that an important task in analyzing this complex phase-space structure lies in finding the gravitationally bound substructures that orbit within the virialized regions of the halos.

We address this complex problem with our SUBFIND algorithm (Springel et al., 2001a) which finds substructures using a topological excursion set method. Based on local dark matter density estimates calculated with the SPH kernel interpolation approach for all high resolution particles, we first identify a set of subhalo candidates, which are locally overdense structures found within a given input group of particles identified with a FOF (friends-of-friends) group finder (Davis et al., 1985). These are then subjected to a gravitational unbinding procedure that iteratively eliminates all unbound particles. Provided more than 20 bound particles remain, we record the particle group as a genuine subhalo in our group catalogue. For each subhalo, we calculate a number of physical properties such as the maximum circular velocity, spin and velocity dispersion, and we store the particles in order of the gravitational binding energy, which is useful for tracking subhalos between simulation outputs at different times. We have fully parallelized the SUBFIND and FOF algorithms for distributed memory systems and inlined them in our simulation code GADGET-3. Thus group-finding can be done on the fly during the simulation, if desired. This is often advantageous as these calculations are computationally quite intense and require equally large memory as the dynamical simulation code itself.

The density values used by SUBFIND were based on SPH density estimates ρ_i with smoothing lengths h_i that satisfy the implicit equation $(4\pi/3)h_i^3\rho_i = 64\,m_{\rm p}$ (Springel & Hernquist, 2002), where $m_{\rm p}$ is the particle mass and an effective neighbour number of 64 was adopted. In order to test the sensitivity of inferred dark matter annihilation rates to the dark matter density estimator (see Springel et al., 2008), we have also calculated densities based on a three-dimensional Voronoi tessellation of the simulation volume, where the density estimate was defined as the mass of a particle divided by its Voronoi volume. To construct the Voronoi tessellation, we have written a parallel code that can rapidly calculate the Delaunay triangulation, and from it its topological dual, the Voronoi tessellation.

As an illustration of the extreme dynamic range of our simulation set and the degree of numerical convergence between the different resolutions, we show in Figure 4 the spherically averaged density profiles for the five simulations of the 'Aq-A' halo. In each case, we draw the measured density profile as a thick solid line down to the smallest radius where convergence is expected based on the criteria of Power et al. (2003), and we continue the measurements as thin lines for scales where the force law is unaffected by the gravitational softening. Power et al. (2003) have shown that convergence of the density profile at a given radius requires that the two-body relaxation time at this radius be larger than the Hubble time. This condition can be cast into the form

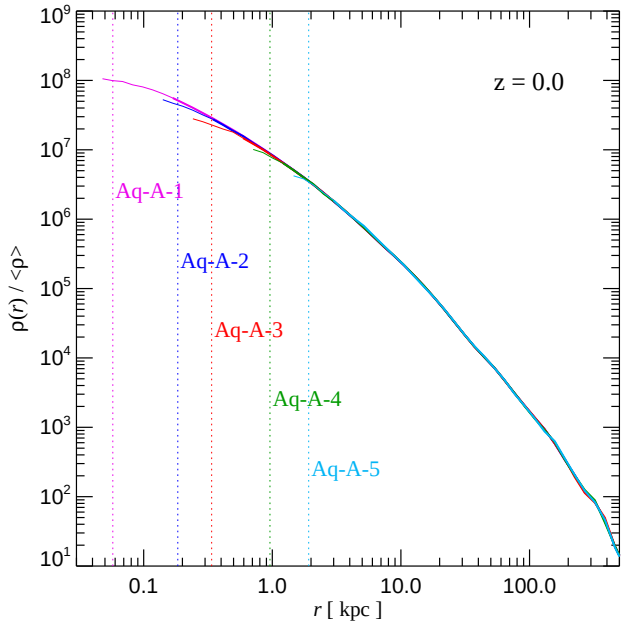

Figure 4. Spherically averaged density profile of the Aq-A halo at $z = 0$, at different numerical resolutions. Each of the profiles is plotted as a thick line for radii that are expected to be converged according to the resolution criteria of Power et al. (2003). These work very well for our simulation set. We continue the measurements as thin solid lines down to $2\,\epsilon$, where ϵ is the Plummer-equivalent gravitational softening length in the notation of Springel et al. (2001b). The dotted vertical lines mark the scale $2.8\,\epsilon$, beyond which the gravitational force law is Newtonian. The mass resolution changes by a factor of 1835 from the lowest to the highest resolution simulation in this series. Excellent convergence is achieved over the entire radial range where it is expected.

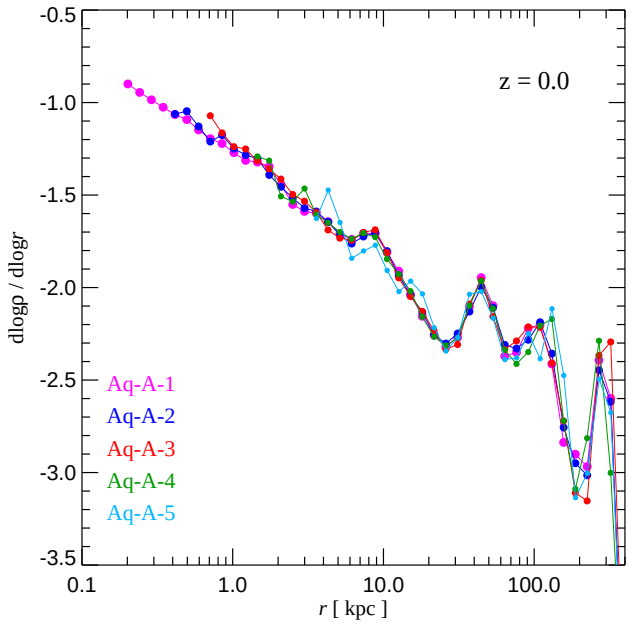

Figure 5. Local logarithmic slope of the density profiles as a function of radius for the Aq-A halo simulated at different numerical resolution. Only the radial region that should be converged according to the criteria of Power et al. (2003) is shown. Note that the large fluctuations in the outer parts are caused by substructures but nevertheless reproduce well between simulations. In this regime, we expect significant halo-to-halo scatter.

$$\frac{\sqrt{200}}{8}\frac{N(r)}{\ln N(r)}\left(\frac{\overline{\rho}(r)}{\rho_{\rm crit}}\right)^{-1/2} \geq 1, \qquad (3)$$

where $N(r)$ is the number of particles inside r, and $\overline{\rho}(r)$ is the average enclosed density. Note that this form of the convergence criterion is in principle also applicable to dark matter subhalos (see below), but in this regime it has not been empirically validated so far.

We find that there is very good agreement between the densities and enclosed masses for all radii larger than the convergence radius estimated in this way. The quality of this convergence is impressively demonstrated by Figure 5, where we show the local logarithmic slope of the density profile, for the radial range where convergence is expected according to the Power criterion. There are some large fluctuations of the local slope in the outer parts of the halo, caused by substructures, which are remarkably well reproduced at the different resolutions. In the more relaxed inner regions, the local logarithmic slope varies smoothly with radius. In particular, it becomes gradually shallower towards the centre, as suggested by Navarro et al. (2004). In fact, the local slope becomes clearly shallower than -1 at the innermost converged radius. This has important implications for the structure of the central cusp which will be analyzed in full detail in Navarro et al. (2008, in preparation). For the rest of this paper, we focus on an analysis of the dark matter substructures.

3 SUBSTRUCTURE ABUNDANCE AND SPATIAL DISTRIBUTION

In this section, we investigate the abundance of dark matter substructures as measured by the SUBFIND algorithm. All our substructures consist of particle groups that are gravitationally self-bound and are overdense with respect to the local background. Every simulation particle can be part only of one subhalo, but we are able to detect substructure within substructure (see below). We count substructures down to a minimum of 20 bound particles.

3.1 Subhalo counts and substructure mass fraction

In Figure 6, we show the differential abundance of subhalos by mass (i.e. the number of subhalos per unit mass interval) in our 'A' halo within r_{50}, and we compare results for simulations of the same object at different mass resolution. For masses above $\sim 5 \times 10^8\,{\rm M}_\odot$, the number of subhalos is small and large halo-to-halo scatter may be expected (see below). However, for lower masses a smooth mass spectrum is present that is well described by a power law over many orders of magnitude. Multiplication by $M_{\rm sub}^2$ compresses the vertical scale drastically, so that the slope of this power-law and deviations from it can be better studied. This is shown in the bottom panel of Figure 6. We see that resolution effects become noticeable as a reduction in the number of objects at masses below a few hundred particles, but for sufficiently well resolved subhalos, very good convergence is reached. There is good evidence from the fully converged

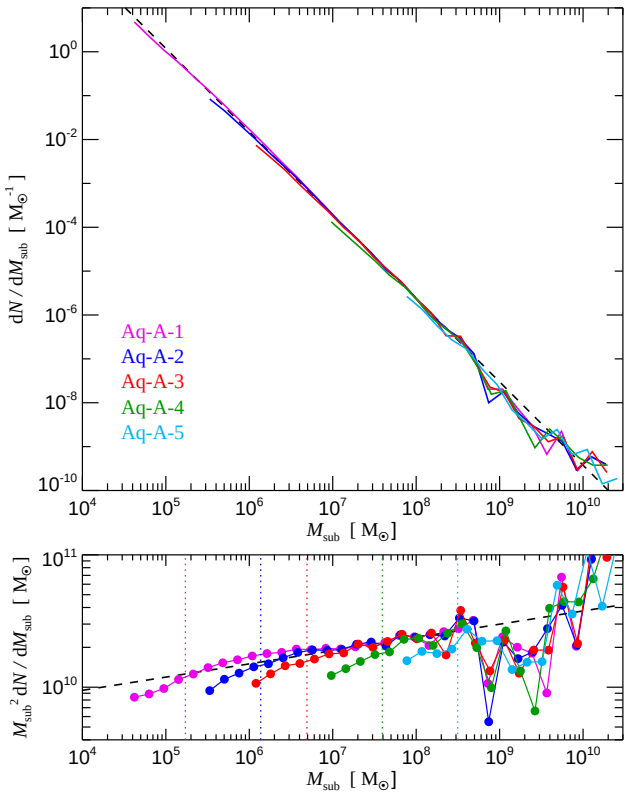

Figure 6. Differential subhalo abundance by mass in the 'A' halo within the radius r_{50}. We show the count of subhalos per logarithmic mass interval for different resolution simulations of the same halo. The bottom panel shows the same data but multiplied by a factor $M_{\rm sub}^2$ to compress the vertical dynamic range. The dashed lines in both panels show a power-law $\mathrm{d}N/\mathrm{d}M \propto M^{-1.9}$. For each of the resolutions, the vertical dotted lines in the lower panel mark the masses of subhalos that contain 100 particles.

part of the differential mass function that it exhibits a true power-law behaviour, and that the slope of this power law is shallower than -2, though not by much. Our results are best fit by a power law $\mathrm{d}N/\mathrm{d}M \propto M^{-1.9}$, the same slope found by Gao et al. (2004), but significantly steeper than Helmi et al. (2002) found for their rich cluster halo. The exact value obtained for the slope in a formal fit varies slightly between -1.87 and -1.93, depending on the mass range selected for the fit; the steepest value of -1.93 is obtained when the fit is restricted to the mass range $10^6\,\mathrm{M}_\odot$ to $10^7\,\mathrm{M}_\odot$ for the Aq-A-1 simulation.

The small tilt of the slope $n = -1.9$ away from -2 is quite important. For $n = -2$, the total predicted mass in substructures smaller than a given limit m_0 would be logarithmically divergent when extrapolated to arbitrarily small masses. If realized, this might suggest that there is no smooth halo at all, and that ultimately all the mass is contained in subhalos. However, even for the logarithmically divergent case the total mass in substructures does not become large enough for this to happen, because a sharp cut-off in the subhalo mass spectrum is expected at the thermal free-streaming limit of the dark matter. Depending on the specific particle physics model, this cut-off lies around an Earth mass, at $\sim 10^{-6}\,\mathrm{M}_\odot$, but could be as low as $10^{-12}\,\mathrm{M}_\odot$ in certain scenarios (Hofmann et al., 2001; Green et al., 2004).

Our measured mass function for the 'A' halo is well approximated by

$$\frac{\mathrm{d}N}{\mathrm{d}M} = a_0 \left(\frac{M}{m_0}\right)^n , \qquad (4)$$

with $n = -1.9$, and an amplitude of $a_0 = 8.21 \times 10^7/M_{50} = 3.26 \times 10^{-5}\,\mathrm{M}_\odot^{-1}$ for a pivot point of $m_0 = 10^{-5}\,M_{50} = 2.52 \times 10^7\,M_\odot$. This means that the expected total mass in all subhalos less massive than our resolution limit $m_{\rm res}$ is

$$M_{\rm tot}(<m_{\rm res}) = \int_{m_{\rm lim}}^{m_{\rm res}} M \frac{\mathrm{d}N}{\mathrm{d}M}\mathrm{d}M = \frac{a_0}{n+2}\,\frac{m_{\rm res}^{n+2} - m_{\rm lim}^{n+2}}{m_0^n} , \qquad (5)$$

where $m_{\rm lim}$ is the thermal dark matter limit. For $m_{\rm lim} \to 0$ and our nominal subhalo resolution limit of $m_{\rm res} = 3.24 \times 10^4\,\mathrm{M}_\odot$ in the Aq-A-1 simulation, this gives $M_{\rm tot} = 1.1 \times 10^{11}\,\mathrm{M}_\odot$, corresponding to about 4.5% of the mass of the halo within r_{50}. While non-negligible, this is considerably smaller than the total mass in the substructures that are *already resolved* by the simulation. The latter is 13.2% of the mass within r_{50} for the Aq-A-1 simulation. We hence conclude that despite the very broad mass spectrum assumed in this extrapolation, the total mass in subhalos is still dominated by the most massive substructures, and an upper limit for the total mass fraction in subhalos is $\sim 18\%$ within r_{50} for the 'Aq-A' halo.

We caution, however, that the extrapolation to the thermal limit extends over 10 orders of magnitude! This is illustrated explicitly in Figure 7, where we show the mass fraction in substructures above a given mass limit, combining the direct simulation results with the extrapolation above. We also include an alternative extrapolation in which a steeper slope of -2 is assumed. In this case, the total mass fraction in substructures would approximately double if the thermal limit lies around one Earth mass. If it is much smaller, say at $m_{\rm lim} \sim 10^{-12}\,\mathrm{M}_\odot$, the mass fraction in substructure could grow to $\sim 50\%$ within r_{50}, still leaving room for a substantial smooth halo component. Notice, however, that within 100 kpc even this extreme extrapolation results in a substructure mass fraction of only about 5%. Most of the mass of the inner halo is smoothly distributed.

Within r_{50} the mass fraction in resolved substructures varies around 11% for our 6 simulations at resolution level 2, each of which has at least 160 million particles in this region. Table 2 lists these numbers, which are 12.2% (Aq-A-2 simulation), 10.5% (Aq-B-2), 7.2% (Aq-C-2), 13.1% (Aq-D-2), 10.8% (Aq-E-2), and 13.4% (Aq-F-2). This gives an average of 11.2% within r_{50} down to the relevant subhalo mass resolution limit, $\sim 2 \times 10^5\,\mathrm{M}_\odot$. This is similar to the substructure mass fractions found by earlier work on galaxy cluster halos (e.g. Ghigna et al., 1998; Springel et al., 2001a; De Lucia et al., 2004) and Galaxy-sized halos (Stoehr et al., 2003) once the different limiting radius (r_{200} instead of r_{50}) is corrected for. However, it is larger than the 5.3% inside r_{50} reported by Diemand et al. (2007a) for a Milky Way-sized halo.

In Figure 8, we compare the differential subhalo mass functions of these six halos, counting the numbers of subhalos as a function of their mass normalized to the M_{50} of their parent halo. Interestingly, this shows that at small subhalo masses the subhalo abundance per unit halo mass shows very little halo-to-halo scatter. In fact, the mean differential abundance is well fit by equation (4) with the parameters

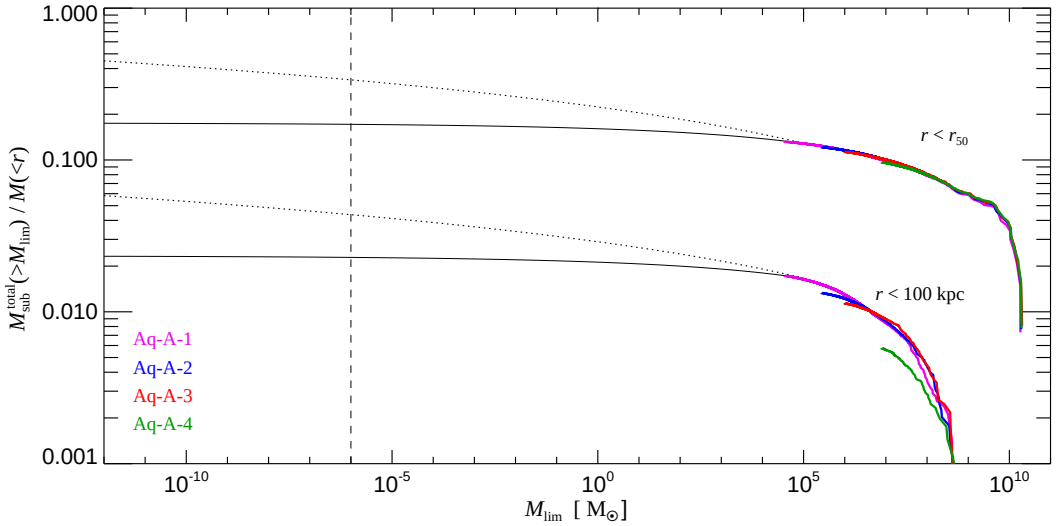

Figure 7. Expected mass fraction in subhalos as a function of the limiting mass $M_{\rm lim}$, inside r_{50} (top curves) and inside 100 kpc (bottom curves). The solid thin lines show an extrapolation of the direct simulation result with an $n = -1.9$ power-law for the differential subhalo mass function. In this case, the total substructure mass converges at the low-mass end. The dotted lines show the prediction for the logarithmically divergent case, $n = -2$. In this case, we would expect the mass in substructures down to an Earth mass (vertical dashed line) to be about twice what we can resolve directly. This mass is a reasonable estimate for the thermal free-streaming limit in many supersymmetric theories where the dark matter particle is a neutralino. However, the parameters of these theories are sufficiently uncertain that the thermal limit could lie as low as $10^{-12}\,{\rm M}_\odot$. Even in this case, the lumpy component of the halo would still be subdominant within r_{50}, and would be a small fraction of the total mass of $9.32 \times 10^{11}\,{\rm M}_\odot$ within 100 kpc.

given above, and the *rms* halo-to-halo scatter in the normalization is only $\sim 8\%$.

In Table 2, we also list a few other basic structural properties of our halos, namely their maximum circular velocity $V_{\rm max}$, the radius $r_{\rm max}$ at which this velocity is attained, a simple measure for halo concentration, and the redshift at which the halo formed. One way to characterize the concentration of a halo is to express the mean overdensity within $r_{\rm max}$ in units of the critical density. This corresponds to the definition

$$\delta_V = \frac{\overline{\rho}(r_{\rm max})}{\rho_{\rm crit}} = 2\left(\frac{V_{\rm max}}{H_0\, r_{\rm max}}\right)^2. \qquad (6)$$

We can relate this quantity to a more familiar concentration measure based on the NFW density profile:

$$\rho = \frac{\rho_s}{(r/r_s)(1+r/r_s)^2}, \qquad (7)$$

where ρ_s and r_s are a characteristic density and radius respectively. Assuming this profile shape, the pair of values $V_{\rm max}$ and $r_{\rm max}$ are sufficient to determine the density profile uniquely. The characteristic NFW overdensity δ_c is then

$$\delta_c = \frac{\rho_s}{\rho_{\rm crit}} = 7.213\,\delta_V, \qquad (8)$$

which can be converted to the NFW concentration c through the equation

$$\delta_c = \frac{200}{3}\frac{c^3}{\ln(1+c) - c/(1+c)}. \qquad (9)$$

We list the "NFW" concentrations calculated in this way as $c^*_{\rm NFW}$ in Table 2. We note however that fits to the full density profile may yield slightly different results, since in this case the circular velocity curve of the fit will not necessarily peak exactly at $r = r_{\rm max}$.

Defining a precise value for the total mass of a subhalo requires an operational definition of its 'outer edge'. Different substructure detection algorithms define different effective boundaries and so produce systematically different total mass estimates. It may therefore be more robust to count subhalos as a function of their peak circular velocity, which typically lies well within the object and so is insensitive to definitions of its edge. Note, however, that in small systems maximum circular velocity estimates can be more sensitive to numerical resolution effects than total mass estimates.

In Figure 9, we show the cumulative abundance of subhalos as a function of maximum circular velocity for our different resolution simulations of Aq-A. Again, there is good convergence. Indeed, at the massive end, the curves lie essentially on top of each other, showing that we are really seeing the *same* subhalos, and that they are reproduced with the *same* maximum circular velocity in all the simulations. This suggests that we are also achieving good convergence for the internal structure of individual subhalos, an issue that we will investigate further below.

However, it is noticeable that the individual measurements for the velocity functions peel away from their higher resolution counterparts comparatively early at low velocities, which suggests worse convergence than found for the subhalo mass functions at the low mass end. This behaviour can be understood as an effect of the gravitational softening length ϵ, which lowers the maximum circular velocities of subhalos for which $r_{\rm max}$ is not much larger than ϵ. To estimate the strength of this effect, we can imagine that the gravitational softening for an existing subhalo is adiabat-

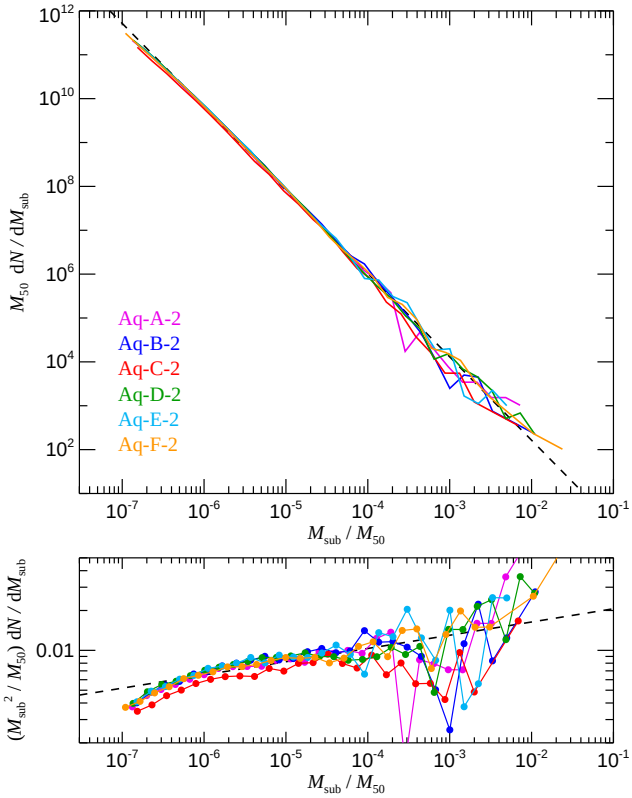

Figure 8. Differential subhalo abundance by mass for our six halos simulated at resolution level 2. We here count all subhalos inside r_{50} and plot their abundance as a function of $M_{\rm sub}/M_{50}$. We see that at low mass the abundance of subhalos is universal to good accuracy when their mass is expressed in units of the mass of their parent halo. The bottom panel shows the same data but multiplied by a factor $M_{\rm sub}^2$ to compress the vertical dynamic range. The dashed lines in both panels show the power-law $\mathrm{d}N/\mathrm{d}M \propto M^{-1.9}$.

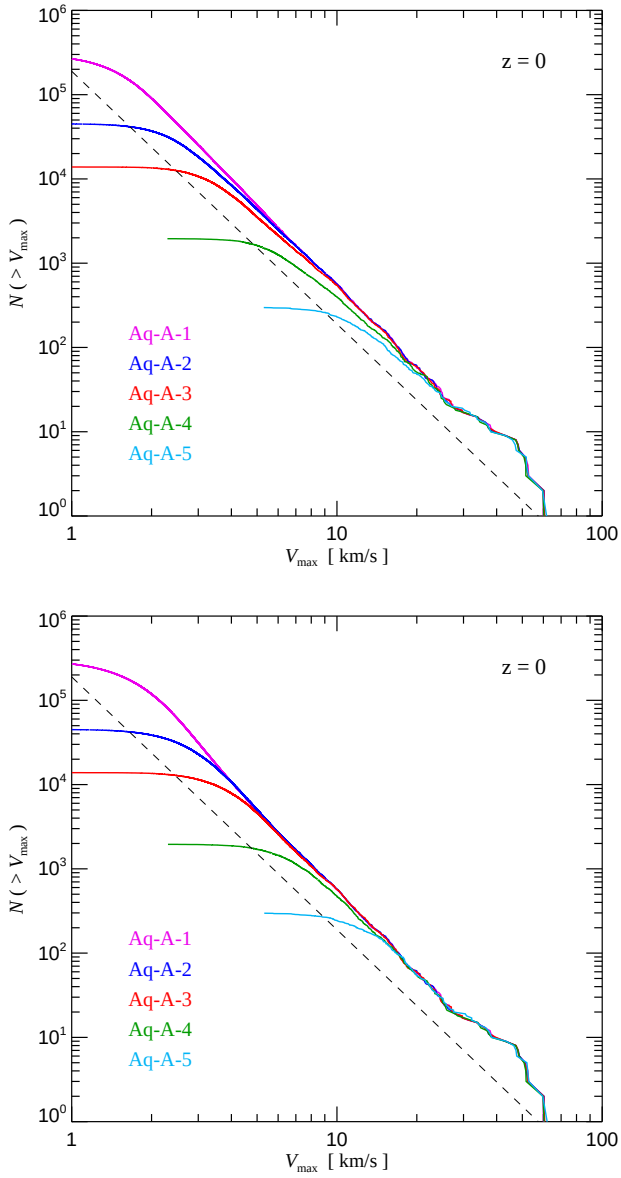

Figure 9. Cumulative subhalo abundance as a function of maximum subhalo circular velocity. The top panel shows the raw measurements from the simulations, while in the bottom panel, we have applied the correction of equation (10) to compensate approximately for the impact of the gravitational softening on $V_{\rm max}$. We show results for 5 simulations of the Aq-A halo carried out with differing mass resolution. The dashed line is the fitting function given for their own simulations by Reed et al. (2005), which also accurately matches the result for the 'Via Lactea I' simulation (Diemand et al., 2007a). This is clearly inconsistent with our own data.

ically lowered from ϵ to zero. The angular momentum of individual particle orbits is then an adiabatic invariant. Assuming for simplicity that all particles are on circular orbits, and that the gravitational softening can be approximated as a Plummer force with softening length ϵ, the expected change of the maximum circular velocity is then

$$V'_{\rm max} = V_{\rm max}\,[1 + (\epsilon/r_{\rm max})^2]^{1/2}. \qquad (10)$$

In the lower panel of Figure 9, we plot the cumulative velocity functions for these corrected maximum circular velocities. Clearly, the measurements line up more tightly down to lower $V_{\rm max}$, demonstrating explicitely that the convergence in the number of objects counted as a function of (corrected) circular velocity is in principle as good as that counted as a function of mass. Note that a similar correction can also be applied to the measured $r_{\rm max}$ values. However, for the remainder of this paper, we focus on the raw measurements from the simulations without applying a gravitational softening correction.

The dashed line in Figure 9 shows the fit which Reed et al. (2005) quote for the subhalo abundance as a function of maximum circular velocity in their own simulations, $N(>V_{\rm max}) = (1/48)(V_{\rm max,sub}/V_{\rm max,host})^{-3}$. Diemand et al. (2007a) found this formula to fit the results from their own Via Lactea I simulation very well. Figure 9 thus confirms the indication from subhalo mass fractions that our simulations show substantially more substructure than reported for Via Lactea I. This is particularly evident at lower subhalo masses which are unaffected by the small number effects which cause scatter in the abundance of massive subhalos. With the help of J. Diemand and his collaborators, we have checked that this abundance difference is not a result of

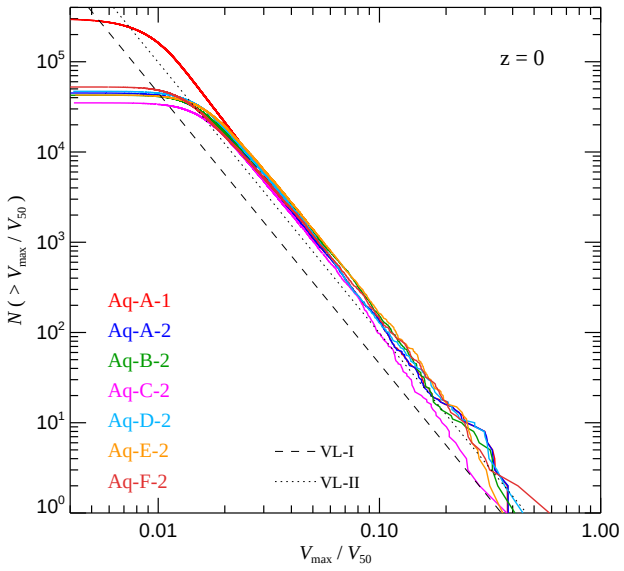

Figure 10. Cumulative subhalo abundance as a function of maximum subhalo circular velocity in units of the circular velocity of the main halo at r_{50}. We show results for all 6 of our halos at resolution level 2, and in addition we include our highest resolution result for the Aq-A-1 run. For comparison, we overplot fitting functions for the Via Lactea I and Via Lactea II simulations (Diemand et al., 2007a, 2008), appropriately rescaled from a normalization to $V_{\rm max,host}$ to one by $V_{\rm 50,host}$.

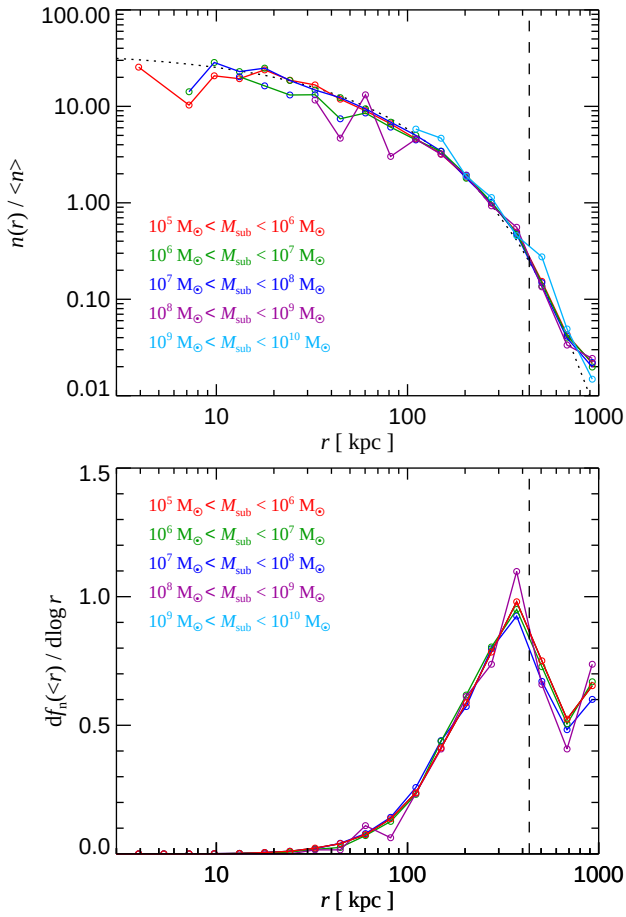

Figure 11. Subhalo number density profiles for different subhalo mass ranges in the Aq-A-1 simulation. In the top panel, the number density profiles for 5 logarithmic mass bins are shown, normalized to the mean number density within r_{50} (vertical dashed line). The profile shape appears independent of subhalo mass, and is well fit by an Einasto profile with $\alpha = 0.678$ and $r_{-2} = 199\,{\rm kpc} = 0.81\,r_{200}$. The bottom panel shows the number fraction of subhalos per logarithmic interval in radius, on a linear-log plot. The area under the curves is proportional to subhalo number, showing that most subhalos are found in the outermost parts of the halo.

the different subhalo detection algorithms used in our two projects.

We do not think that this discrepancy can be explained by halo-to-halo scatter since it is much larger than the variation in substructure abundance among our own sample of halos. This is demonstrated in Figure 10, which shows the cumulative subhalo abundance distributions within r_{50} as a function of maximum subhalo circular velocity for all our resolution level 2 halos. We plot subhalo count against subhalo maximum circular velocity normalized to V_{50}, the circular velocity of the main halo at r_{50}. Because the slope of the abundance curve is very close to -3, this is equivalent to plotting subhalo count normalized by the total parent halo mass within r_{50} (which is proportional to V_{50}^3) against subhalo maximum circular velocity. There is remarkably little scatter between our simulations when normalized in this way; the *rms* scatter in amplitude in the power-law regime is around 10%. The figure also shows the substructure abundance reported for the Via Lactea I (dashed) and II (dotted) simulations (Diemand et al., 2007a, 2008), after rescaling to the normalization we prefer here.‡. There is a difference of a factor of 3.1 between the mean abundance of small subhalos in our simulations and in 'Via Lactea I'. The Diemand et al. (2008) abundance for Via Lactea II differs substantially from that for Via Lactea I and is much closer to our results. Nevertheless, the abundance of small subhalos in Via Lactea II is still 31% lower than the mean for our set of 6 halos, which is more than three times the *rms* scatter in abundance between our halos.

These results lead us to disagree with the assertion by Madau et al. (2008) and Diemand et al. (2008) that differences of this magnitude lie within the halo-to-halo scatter. Instead, the substantial difference between 'Via Lactea I' and Via Lactea II' must have a systematic origin. We also think it unlikely that the higher abundance in our simulations reflects the small differences in the background cosmology assumed in the two projects, as suggested by Madau et al. (2008), even though this is a possibility we cannot exclude. For example, the Via Lactea simulations assumed a lower value for σ_8 than we used, and we believe that lowering σ_8 should result in slightly *more* substructure in objects

‡ Note that $V_{\rm 50,host}$ unambiguously characterizes the enclosed mass within r_{50}, the region in which subhalos are counted. This is not the case for $V_{\rm max,host}$, the velocity scale chosen by Diemand et al. (2008), because it is additionally affected by halo concentration.

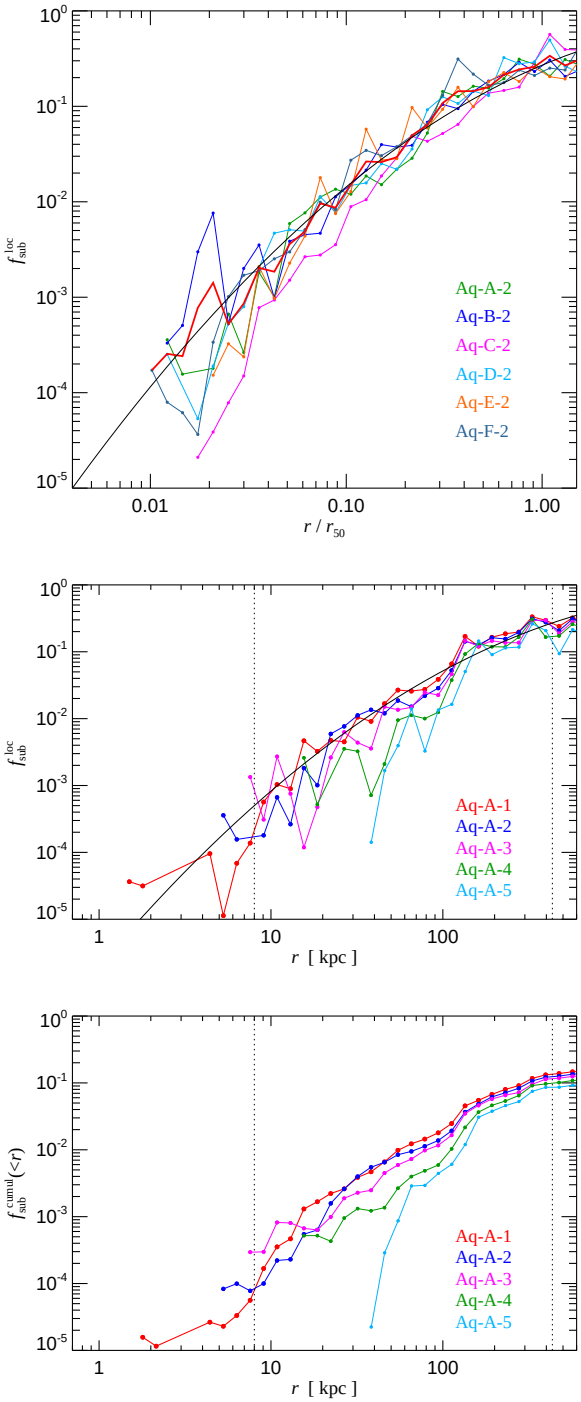

Figure 12. The mass fraction in subhalos as a function of radius. In the top panel, we show results for the *local* mass fraction in substructures for our six different halos, as a function of radius normalized by r_{50}. The thick solid line shows the average of all the runs. In the middle panel, we consider the same quantity for the different resolution simulations of the Aq-A halo, while in the bottom panel we show the corresponding *cumulative* substructure fractions in the Aq-A halo. The solid line in the two upper panels is an empirical fit with a slowly running power law index. The vertical dotted lines at 8 kpc in the middle and bottom panels mark the position of the Solar circle; here the expected local mass fraction in subhalos has dropped well below 10^{-3}. The outer vertical dotted lines mark r_{50} for the Aq-A halo.

of given mass, simply because these halos then tend to form more recently which increases the number of surviving subhalos within them (e.g. De Lucia et al., 2004). We have explicitly confirmed this effect by comparing the substructure abundances in the Millennium simulation (with $\sigma_8 = 0.9$) with those in the simulations of Wang et al. (2008), which used the same cosmology except for taking $\sigma_8 = 0.722$. On the other hand, the different tilt assumed for the primoridial power spectrum of the Via Lactea II simulation may have reduced the subhalo abundance and could perhaps be responsible for the difference (Zentner & Bullock, 2003).

We note that the small halo-to-halo scatter in substructure abundance which we find also contradicts the recent suggestion by Ishiyama et al. (2007) that the halo-to-halo variation in subhalo abundance could be very large, and that the apparent paucity of dwarfs surrounding the Milky Way might simply reflect the fact that our Galaxy happens to live in a low density environment.

3.2 The spatial distribution of subhalos

In Figure 11, we show the radial distribution of subhalos of different mass within our Aq-A-1 simulation. In the top panel, we plot the number density profile for different subhalo mass ranges, each normalized to the mean number density of subhalos of this mass within r_{50}. The number density of subhalos increases towards halo centre, but much more slowly than the dark matter density, consistent with previous work (e.g. Ghigna et al., 1998; Gao et al., 2004; Nagai & Kravtsov, 2005; Diemand et al., 2004, 2007a). As a result, most subhalos of a given mass are found in the outer parts of a halo, even though the number density of subhalos is highest in the central regions. Another view of this behaviour is given in the bottom panel of Figure 11, which histograms the abundance of subhalos as a function of log radius so that the area under the curves is proportional to the total number of subhalos. Clearly, the vast majority of subhalos are found between ~ 100 kpc and the outer radius of the halo.

Perhaps the most remarkable aspect of Figure 11 is that there appears to be no trend in the shape of the number density profiles with subhalo mass. Previous work has already hinted at this behaviour (Diemand et al., 2004; Ludlow et al., 2008), which is here confirmed with much better statistics and over a much larger dynamic range in mass. We note that this disagrees with a tentative finding by De Lucia et al. (2004), who suggested that more massive substructures have a radial profile that is more strongly antibiased with respect to the mass than that of low mass subhalos. Like Ludlow et al. (2008) we find that the number density profile is well described by an Einasto profile (a fit to our measurements yields a shape parameter $\alpha = 0.678$ and scale radius $r_{-2} = 199\,{\rm kpc} = 0.81\,r_{200}$). It is thus tempting to conjecture that this behaviour continues to (arbitrarily) small subhalo masses. If true, an interesting corollary is that there must be a smooth dark matter component which dominates the inner regions of halos. Only the outer parts may have a substantial mass fraction in lumps (see also Figure 7). This contrasts with previous speculations (Calcáneo-Roldán & Moore, 2000; Moore et al., 2001) that all the mass of a halo may be bound in subhalos.

Further light on this question is shed by Figure 12,

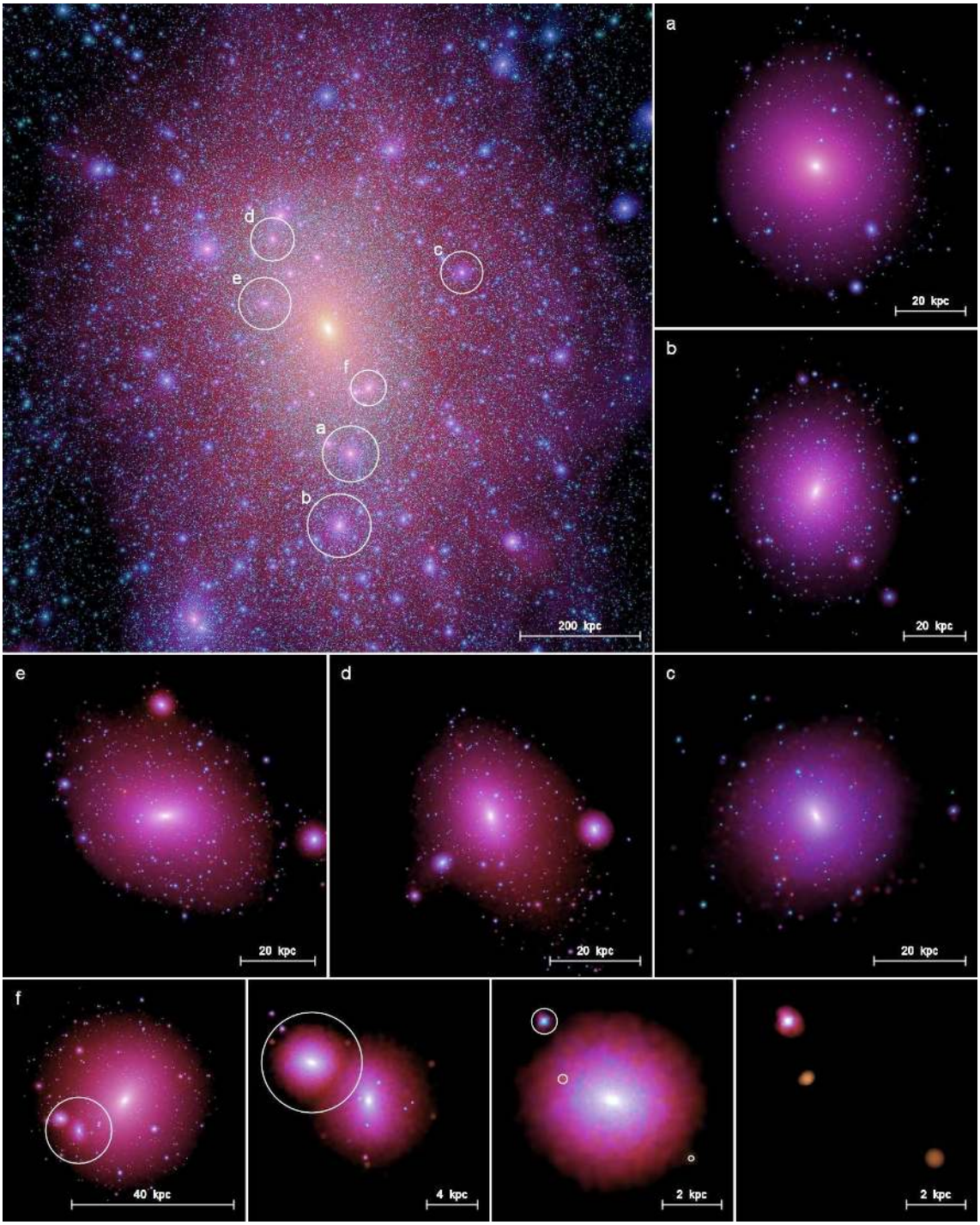

Figure 13. Images of substructure within substructure. The top left panel shows the dark matter distribution in a cubic region of side $2.5 \times r_{50}$ centred on the main halo in the Aq-A-1 simulation. The circles mark six subhalos that are shown enlarged in the surrounding panels, and in the bottom left panel, as indicated by the labels. All these first generation subhalos contain other, smaller subhalos which are clearly visible in the images. SUBFIND finds these second generation subhalos and identifies them as daughter subhalos of the larger subhalos. If these (sub-)subhalos are large enough, they may contain a third generation of (sub-)subhalos, and sometimes even a fourth generation. The bottom panels show an example of such a situation. The subhalo shown on the bottom left contains another subhalo (circled) which is really made up of two main components and several smaller ones (bottom, second from left). The smaller of the two components is a third generation substructure (bottom, third from left) which itself contains three subhalos which are thus fourth generation objects (bottom right).

where we show the local mass fraction in subhalos as a function of radius. In the top panel, we compare results for our six different halos, with the radial coordinate normalized by r_{50}. While there is some scatter between the different halos, the general behaviour is rather similar and shows a rapid decline of the local mass fraction in substructures towards the inner parts of each halo. The mean of the six simulations (thick red line) is well fit by a gently curving power-law. It can be parameterized by

$$f_{\rm sub} = \exp\left[\gamma + \beta \ln(r/r_{50}) + 0.5\,\alpha \ln^2(r/r_{50})\right], \qquad (11)$$

with parameters $\alpha = -0.36$, $\beta = 0.87$, and $\gamma = -1.31$. This fit is shown in the upper two panels of Figure 12 as a thin black line. The middle panel is the same measurement, but for all the different resolution simulations of the Aq-A halo, while the bottom panel is the corresponding cumulative plot. These two panels give an impression of how well numerical convergence is achieved for this quantity.

An interesting implication from Figure 12 is an estimate of the fraction of the mass in substructures near the Solar Circle (marked by a vertical dashed line). At $r = 8\,$kpc, the expected local mass fraction in substructure has dropped well below 10^{-3}. This measurement appears converged, and accounting for unresolved substructure does not raise the fraction above 10^{-3} (compare Figure 7). The dark matter distribution through which the Earth moves should therefore be mostly smooth, with only a very small contribution from gravitationally bound subhalos.

4 SUBHALOS INSIDE SUBHALOS

In our simulations, we find several levels of substructure within substructure. Figure 13 illustrates this by showing individually 6 of the largest Aq-A-1 subhalos in enlarged frames. Clearly, all of these subhalos have embedded substructures. Sometimes these second-generation subhalos contain a further (third) level of substructure and, in a few cases, we even find a fourth generation of subhalos embedded within these. An example is given in the bottom row of Figure 13, which zooms recursively on regions of the subhalo labeled "f" in the top-left panel. As shown in the bottom-left panel, subhalo "f" has several components, each of which has identifiable sub-components; we are able to identify up to four levels of this hierarchy of substructure in this system. We note that the hierarchy of nested structures is established directly by the recursive nature of the SUBFIND algorithm; at each level, a given substructure and its parent structure are surrounded by a common outer density contour that separates them from the next level in the hierarchy.

It is important to quantify in detail the hierarchical nature of substructure, since this may have a number of consequences regarding indirect and direct dark matter search strategies. Recently, Shaw et al. (2007) suggested that the (sub-)substructure distribution in subhalos might be a scaled version of the substructure distribution in main halos. This claim has been echoed by Diemand et al. (2008), who report roughly equal numbers of substructures inside radii enclosing a mean overdensity of 1000 times the cosmic average value (r_{250} in our notation) and centred at either subhalos or the main halo. This result has been interpreted by Kuhlen et al. (2008) to imply that the (sub-)subhalo abundance per unit mass of a subhalo should be roughly constant and equal to that of the main halo. This, however, seems unlikely because, as we have seen, local substructure abundance is a strong function of radius in main halos, with most of the substructure found in the outer regions.

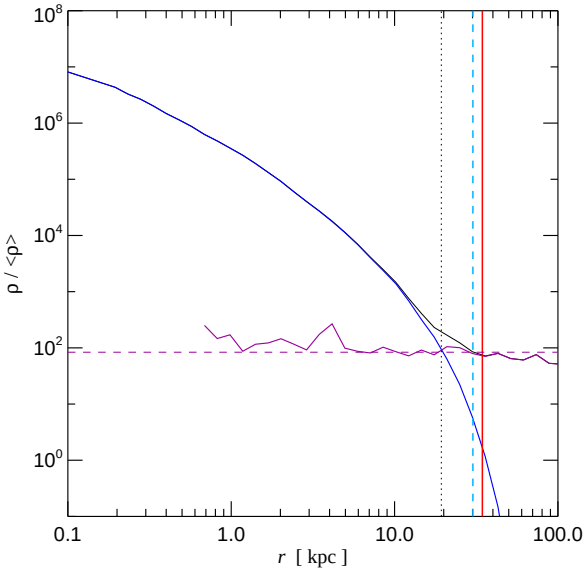

Figure 14. An example of the determination of the subhalo radius $r_{\rm sub}$. The thick blue line shows the spherically averaged density profile of particles identified by SUBFIND as gravitationally bound to the subhalo, while the thin black line is the density profile of all particles. The purple line is the density profile of the difference, i.e. of all particles that are not bound to the subhalo. The dashed horizontal line is the mean local background density $\rho_{\rm loc}$ at the subhalo's location, estimated within the radius marked by the vertical dotted line, which encloses $M_{\rm sub}$ in the profile of the total mass. The red vertical line marks our estimated radius $r_{\rm sub}$, at which point the bound density profile has dropped to $0.02 \times \rho_{\rm loc}$. The dashed blue vertical line shows the estimated tidal radius of the subhalo based on $M_{\rm sub}$.

In this section, we present the first convergence studies ever attempted for (sub-)substructure inside subhalos in order to assess the alleged self-similarity of the substructure hierarchy. We begin by discussing a suitable definition for the outer edge of a subhalo, which allows us to measure the (sub-)substructure mass fractions of subhalos in a consistent manner. We then study the number and mass of sub-subhalos within that radius and compare them with the expectation from self-similarity. In order to compare with recent work by Diemand et al. (2008), we also carry out, for a few subhalos, the same analysis within a radius of fixed overdensity, r_{250}.

4.1 The radius of a subhalo

SUBFIND identifies substructures as locally overdense regions relative to the average background density. It is thus able to find substructures and assign masses to them without large biases throughout most of the halo. The procedure, however, may break down near the centre, where the average density of the main halo may overwhelm even the highest density peak of embedded substructures, leading to poten-

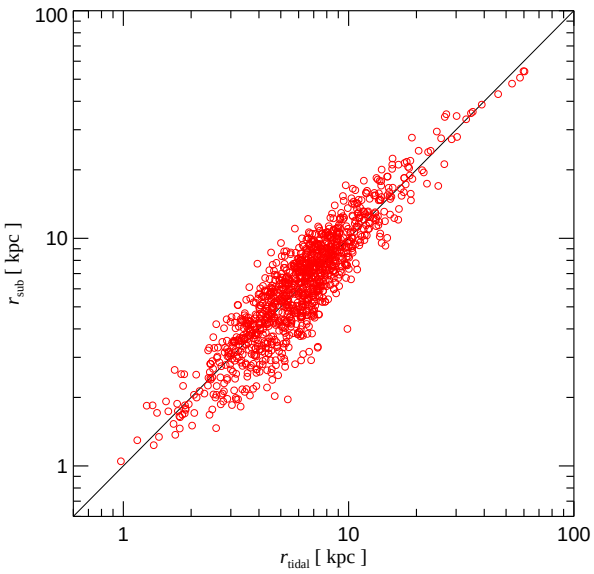

Figure 15. Comparison between estimated subhalo radii and tidal radii for the Aq-A-1 simulation. Only subhalos with at least 10^4 particles have been included in this plot.

tial biases in the masses assigned to subhalos by SUBFIND. It is therefore desirable to find a definition for the radius of a subhalo that is simple and physically meaningful and, at the same time, relatively insensitive to the accuracy with which SUBFIND assigns subhalo masses.

We have settled on the following operational procedure for determining a subhalo radius, $r_{\rm sub}$. Starting from the centre of a particular subhalo, we first measure spherically averaged density profiles for all the mass and for the gravitationally bound mass (as determined by SUBFIND). We then obtain a measure for the local density of the main halo at the position of the subhalo location by: (a) determining the radius r' enclosing total mass equal to $M_{\rm sub}$; (b) determining the amount of unbound mass M' inside this radius (this is simply the difference between $M_{\rm sub}$ and the bound mass within r'); (c) defining $\rho_{\rm loc} = M'/(4\pi r'^3/3)$. With this in hand, we operationally define the bounding radius $r_{\rm sub}$ of the subhalo to be the radius at which the spherically averaged density profile of the bound mass has dropped below $0.02 \times \rho_{\rm loc}$.

The bound density profile drops very steeply near the edge of the subhalo, so changing the prefactor 0.02 has only a minor influence on the radius determined in this way. We found that, with this choice, the edge of the subhalo is robustly determined right at the transition between the falling density profile of the subhalo, and the approximately constant local background density of the halo. Also, this radius tends to agree well with the minimum in the circular velocity curve constructed using *all* the mass around the subhalos's centre. In Figure 14, we show a typical example to illustrate this procedure. Note that the determination of $\rho_{\rm loc}$, and hence the value of $r_{\rm sub}$ obtained through the above procedure, is relatively insensitive to the precise value of $M_{\rm sub}$.

In Figure 15, we show how the subhalo radii determined in this way compare with tidal radii derived from the distances of subhalos to halo centre, and their SUBFIND masses $M_{\rm sub}$. We calculate the tidal radius (Binney & Tremaine, 1987; Tormen et al., 1998) of a subhalo of mass $M_{\rm sub}$ and distance r from the centre of the main halo as

$$r_{\rm t} = \left(\frac{M_{\rm sub}}{[2 - {\rm d}\ln M/{\rm d}\ln r]\, M(<r)} \right)^{1/3} r \qquad (12)$$

where $M(<r)$ is the main halo mass within a sphere of radius r. Reassuringly, there is good agreement between $r_{\rm t}$ and $r_{\rm sub}$ in the mean, with some scatter. This gives us further confidence that our subhalo radii are physically meaningful, and that SUBFIND correctly identifies the self-bound regions of subhalos.

4.2 Matching individual subhalos

In order to study convergence not only of the main halo but also of individual embedded subhalos, we need an appropriate method to identify the *same* subhalo in simulations with different mass resolution. This is less straightforward than it may seem at first, since one cannot expect the subhalo to be at exactly the same *position* in different simulations. When the numerical resolution is changed, small phase offsets build up in the orbits of individual subhalos, causing them to be at slightly different positions in different simulations, even though their histories and their internal structure may agree in detail (see, e.g., Frenk et al., 1999).

One solution to this problem is to match subhalos at very early times, by tracking the particles of a particular subhalo back to the (unperturbed) initial conditions. For each particle, we can then find the closest particle in another realization of the initial conditions created for the *same halo* but at different numerical resolution. These matched particles can then be tracked forward in time in the second simulation to see where they end up. This yields a set of possible subhalo matches in the second simulation, among which the one containing the largest number of matched particles is selected as the partner to the original subhalo. To increase robustness, one may require that the same match be obtained when the procedure is carried out in reverse, i.e. starting with the subhalo in the second simulation.

We have found this procedure to work quite robustly for our simulation set. To speed up the matching procedure in the unperturbed initial conditions, we have successfully applied the following trick. Our IDs are constructed as 63-bit Peano-Hilbert keys (Springel, 2005), i.e. they correspond to positions along a space-filling fractal that tessellates our simulation volume with a fiducial grid of 2^{21} cells per dimension. This corresponds to a comoving spatial resolution of around 65 pc, which is still considerably smaller than the mean particle spacing in the high resolution region, even for the Aq-A-1 simulation. Exploiting the fact that positions that are close on the Peano-Hilbert curve are always close in 3D space (the reverse is, however, not always true), we can accelerate the matching by finding the particle with the nearest Peano-Hilbert key in the second simulation. This always finds a particle that is very close, although it does not guarantee that it is the closest. This procedure turns out to be quite sufficient for the task at hand here.

In Figure 18 we compare properties of subhalos matched in this way in the Aq-A series of simulations. The two panels on the left show the masses and maximum circular velocities

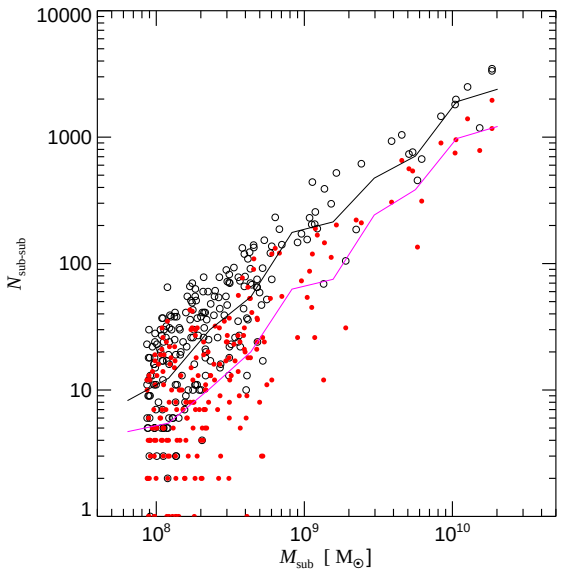

Figure 16. (Sub-)substructure count within subhalos as a function of their mass. The plot includes all subhalos with more than 50,000 particles in the Aq-A-1 simulation. The actual (sub-)subhalo counts for these subhalos are shown as red dots and their average in logarithmically spaced mass bins is indicated by the purple line. Open circles show the (sub-)subhalo count which these same subhalos would have if they were scaled-down copies of the main halo, with the corresponding average indicated as a function of mass by the solid black line. When estimating these predictions, we correct for the lower effective resolution within subhalos in comparison to the main halo by only counting main halo subhalos above the appropriately scaled mass limit.

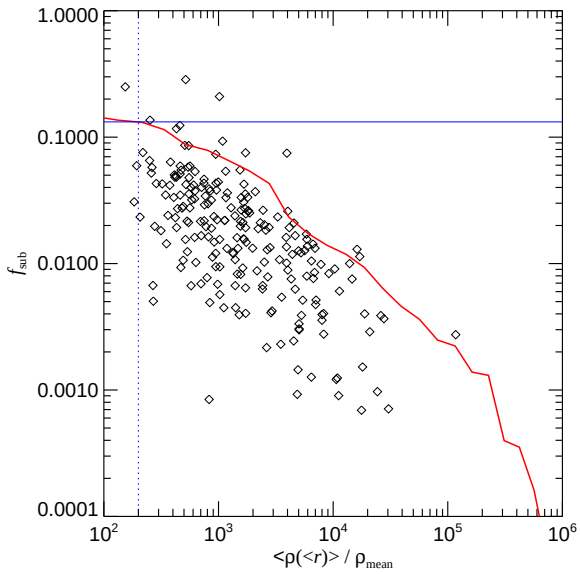

Figure 17. (Sub-)substructure mass fraction in subhalos as a function of their radius within the main halo, expressed as the mean enclosed density in units of the cosmic mean density. The innermost subhalos are thus on the right. The plot includes all subhalos with more than 50,000 particles in Aq-A-1 (shown as symbols). All (sub-)subhalos within the estimated subhalo radius $r_{\rm sub}$ are counted, and their total mass is normalized by the total mass within $r_{\rm sub}$. To be able to compare all measured values of $f_{\rm sub}$ on an equal footing, we add a correction to account for (sub-)subhalos below our resolution limit but above the mass which corresponds to the resolution limit in the main halo after scaling down to each subhalo. The solid red line gives the substructure mass fraction which the subhalos would have if they were scaled down versions of the main halo, but with all material outside the tidal radius removed. The horizontal blue line is the substructure mass fraction for the main halo within r_{50}.

of subhalos in the Aq-A-1, Aq-A-3, and Aq-A-4 simulations in units of the values measured for their counterparts in the Aq-A-2 simulation. Remarkably, the agreement is excellent with a surprisingly small scatter, and there is no obvious systematic offset between the different resolutions. Further analysis of these data is given in Springel et al. (2008), where we show that the maximum circular velocity of subhalos can be trusted in the mean with an accuracy of 10% down to $V_{\rm max} \sim 1.5\,{\rm km\,s^{-1}}$. Convergence for $r_{\rm max}$ is more difficult to achieve, but is still good in the mean down to $r_{\rm max} \sim 165\,{\rm pc}$. In the right panel of Fig. 18 we compare the projected spatial positions of matching subhalos in the Aq-A-1, Aq-A-2, Aq-A-3 and Aq-A-4 simulations. While the agreement for the absolute coordinates is not perfect, especially for subhalo quartets close to the main halo's centre, matching subhalos are generally found quite close together. The mean spatial offset is of order $\sim 30\,{\rm kpc}$, which is much better than we have typically found in our older simulation work (Stoehr et al., 2003). This is a tribute to the improved integration accuracy in GADGET-3, and to the high quality of our initial conditions.

4.3 The abundance of substructures within subhalos

Using our matched sets of subhalos we are now ready to consider the convergence of the properties of substructure inside subhalos. We begin by considering (sub-)substructures within the subhalo radius, $r_{\rm sub}$, and extend the analysis later to regions of fixed overdensity, in order to compare with the results reported by Diemand et al. (2008).

We start by simply counting all subhalos within $r_{\rm sub}$ of a given subhalo's centre and comparing the count with the number expected from the assumption that subhalos are simply scaled-down copies of the main halo. This expected number must be adjusted to take into account that, unlike the main halo, subhalos have a different "edge" ($r_{\rm sub}$), as well as comparatively poorer mass resolution. In practice, the self-similar expected number is computed by considering in the main halo only subhalos with masses exceeding $20\,m_{\rm p}\,M_{\rm main}/M_{r_{\rm sub}}$, where $20\,m_{\rm p}$ is our absolute SUBFIND mass limit for subhalo detection, $M_{\rm main}$ is the main halo's mass within a radius that encloses the same overdensity as that of the subhalo within $r_{\rm sub}$, and $M_{r_{\rm sub}}$ is the *total* mass within $r_{\rm sub}$ of the subhalo's centre.

In Figure 16 we compare the actual (sub-)subhalo counts with the self-similar expectation, as a function of subhalo mass. Interestingly, we always find fewer (sub-)subhalos than expected from the self-similar hypothesis. The suppression in substructure abundance is not uniform; a few subhalos have almost the full expected abundance, while others lie well below it. This is not entirely unexpected, and it is

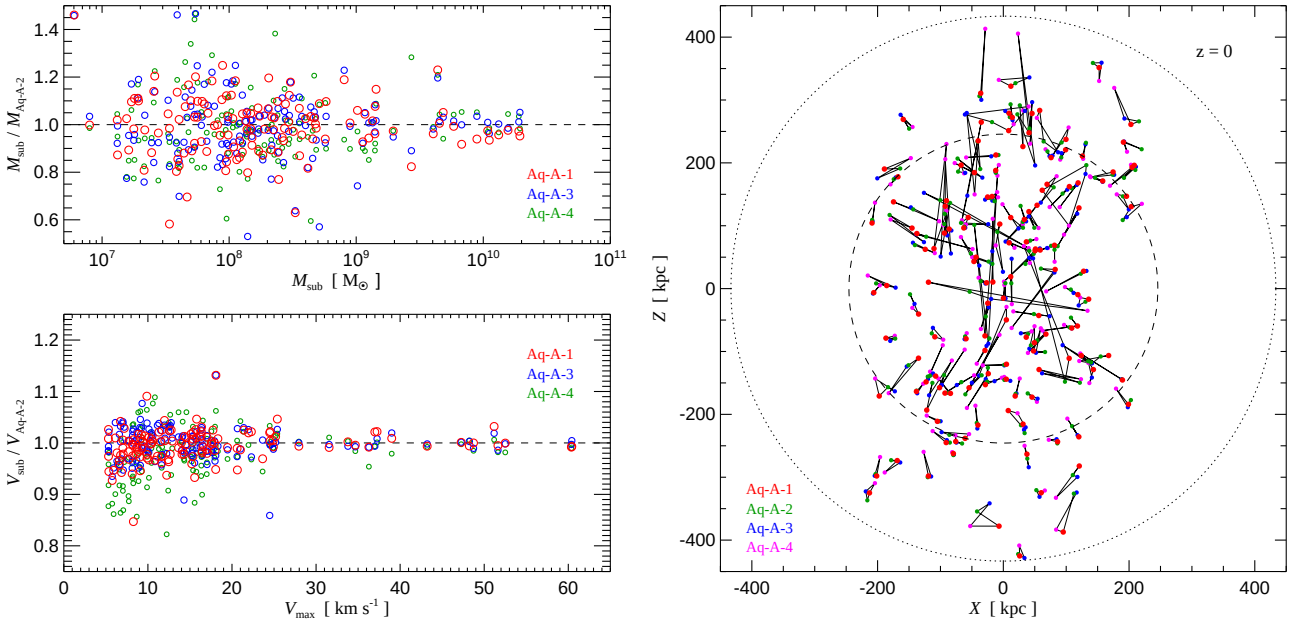

Figure 18. The two panels on the left compare the $M_{\rm sub}$ and $V_{\rm max}$ values of individual matched subhalos in Aq-A-1, Aq-A-2, Aq-A-3, and Aq-A-4. In both panels, the measured values are ratioed against the value found in Aq-A-2, our second highest resolution simulation of the 'A' halo. In the panel on the right, we use small circles to indicate the projected positions of the matched subhalos on the xz-plane. The positions of each subhalo in the 4 different simulations are joined by thin lines. The mean positional off-set between matched subhalos in Aq-A-4 and Aq-A-1 is ~ 54 kpc. This shrinks to 28 and 26 kpc for matches of Aq-A-3 and Aq-A-2 to Aq-A-1, respectively. The inner and outer circles mark r_{200} and r_{50}.

probably related to the time since each subhalo was accreted into the main halo and the extent to which it has lost mass to tides. Typically the number of (sub-)subhalos is a factor of 2 or 3 below that predicted by self-similarity.

The mass fraction of subhalos in the form of embedded substructure provides another way of quantifying (sub-)substructure abundance. To estimate this we simply measure the total mass of all (sub-)subhalos within $r_{\rm sub}$ and divide it by the *total* mass $M(r_{\rm sub})$ contained within this same radius. Because the minimum subhalo size identified by SUBFIND is always 20 particles regardless of the mass of the parent object (main halo or subhalo), we correct the measured cumulative substructure mass by extrapolating the mass function from $20\,m_{\rm p}$ down to $20\,m_{\rm p}\,M(r_{\rm sub})/M_{\rm main}$ using a slope $N(>m) \propto m^{-0.9}$. Note that $M_{\rm main}$ is here the mass of the main halo measured within the radius that encloses an equal mean overdensity as the subhalo within $r_{\rm sub}$.

In Figure 17, we compare the substructure mass fraction of subhalos to those of the main halo. The latter is computed within the radius where the main halo density equals that of the subhalo ($\overline{\rho}(r) = \rho_{\rm sub}$). As shown in Figure 17, computed in this way the main halo prediction is a monotonically decreasing function of $\rho_{\rm sub}$. Interestingly, this line forms an accurate upper bound to the measured substructure mass fractions of subhalos. Close to the line, the self-similar expectation is fulfilled, but the fact that most subhalos lie considerably below the line confirms that substructure is on average significantly under-abundant in subhalos when compared to the main halo.

For completeness, and in order to ease comparison with previous work, we show in Figure 19 the cumulative subhalo abundance for 12 of our more massive subhalos in the Aq-A halo. For the first time, we consider the convergence of the (sub-)substructure mass function for individual subhalos, based on the Aq-A-1, Aq-A-2, and Aq-A-3 simulations and our matched set of subhalos. Here we count all substructures within a sphere (of radius r_{250}) centred on the subhalo, and of mean overdensity 250 times the critical density (and so 1000 times the cosmic mean density, as chosen by Diemand et al., 2008). A further criterion for selecting the subhalos shown in Figure 19 was that their tidal radius r_t should exceed r_{250}, thus ensuring that the region where (sub-)subhalos are counted really lies *inside* the subhalo. Note that this criterion is actually rather restrictive, as it precludes subhalos from study that are at radii $r < r_{250} = 258$ kpc.

The (sub-)subhalos shown in Figure 19 are counted as a function of their mass normalized by M_{250}, the total mass of each subhalo within its own r_{250}. When the substructure in main halos is counted in this way, a near-universal cumulative subhalo mass function is found, as we show explicitly in Figure 20 for our sample of 6 halos simulated at resolution level 2. There is a well-defined mean relationship with little scatter. For reference, we include a power-law fit to this relation in the various panels of Figure 19. Clearly, also in this case most subhalos show a cumulative substructure mass function with similar slope but with a normalization that is typically substantially lower. Only a few subhalos have a substructure abundance which approaches that predicted by scaling our results the main halo.

We may also compare the substructure abundance of subhalos inside r_{250} with that of *field halos* of equal M_{250}, such that both are equally well resolved and biases due to different numerical resolutions are excluded. Figure 21 shows

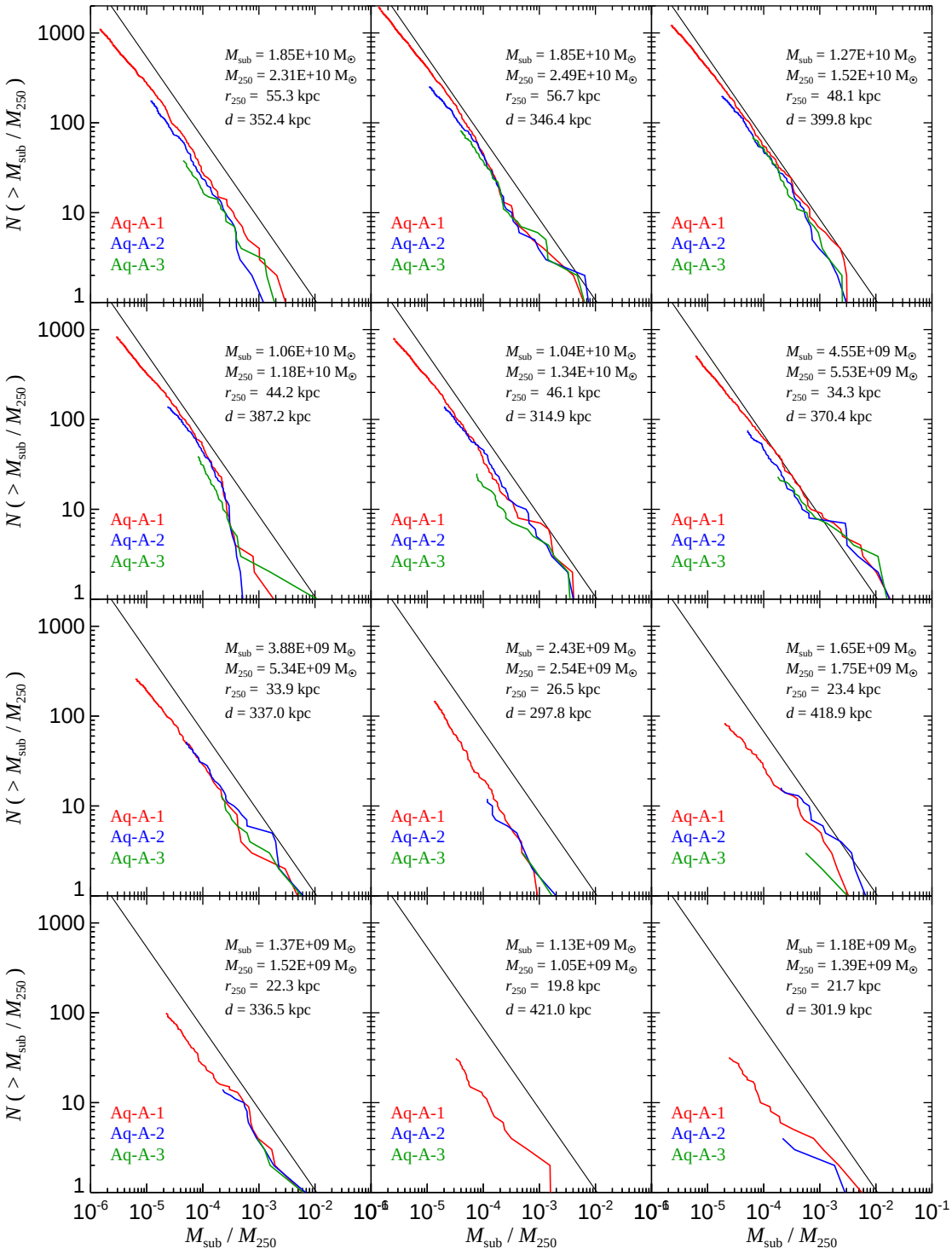

Figure 19. Cumulative mass function of (sub-)subhalos within subhalos. In each panel, we show results for one subhalo, and we compare results for different numerical resolutions, corresponding to simulations Aq-A-1, Aq-A-2 and Aq-A-3. Only substructures within a distance r_{250} of the subhalo centre are counted, and the substructure mass is normalized to the mass within this radius M_{250}. The thin black power-law shows the subhalo abundance of main halos within a radius enclosing the same mean overdensity. The labels in each panel give the subhalo mass $M_{\rm sub}$ as determined by SUBFIND, the values of M_{250} and r_{250}, and the distance d of the subhalo from the centre of the main halo.

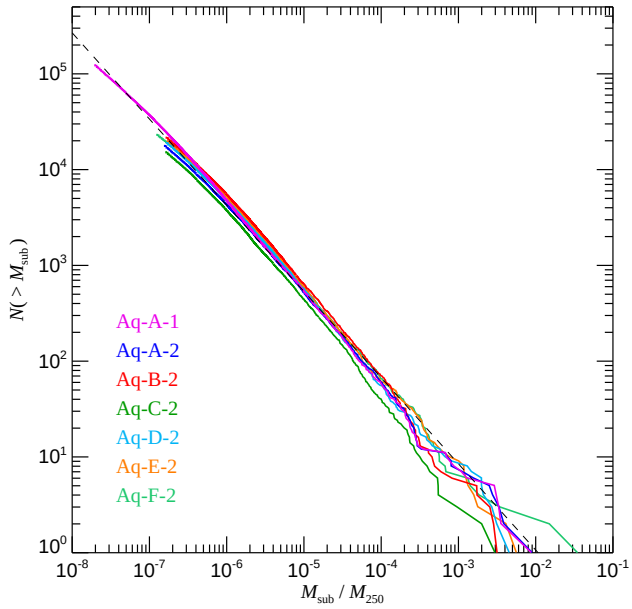

Figure 20. Cumulative subhalo mass function within r_{250} for our 6 different halos at level 2 resolution, as well as for our highest resolution run Aq-A-1. Subhalo masses are measured in units of M_{250} in each case. The dashed line is a fit to the mean mass function.

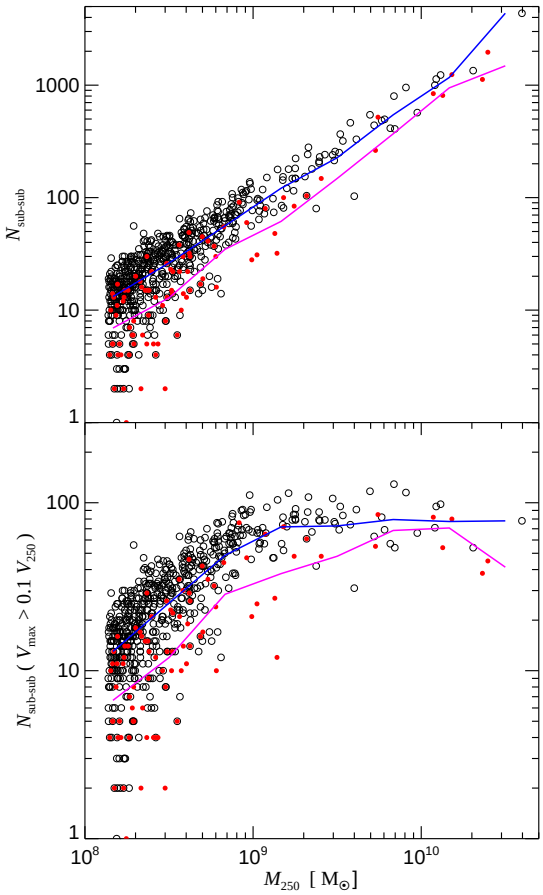

Figure 21. Substructure count in subhalos of Aq-A-1 within r_{250} (red filled circles) compared with field halos (hollow black circles) inside r_{250}, as a function of M_{250}. The top panel shows the substructure count down to our resolution limit, while the bottom panel gives the count above a limiting maximum circular velocity equal to $0.1\,V_{250}$, which effectively measures the amplitude of the subhalo velocity function. The solid lines give averages for independent logarithmic mass bins. We see that there is a systematic offset in the substructure abundance of field halos and genuine subhalos. The downturn of the count above $0.1\,V_{250}$ for masses below $\sim 10^9\,M_\odot$ is due to resolution limitations.

our results for this comparison, both in terms of the count of all substructures down to the resolution limit, and by just counting subhalos with a maximum circular velocity larger then $0.1\,V_{250}$, which effectively measures the amplitude of the (sub-)subhalo velocity function. We here used uncontaminated field halos found in the high-resolution region around the main halo in Aq-A-1, and compared them to subhalos in the outer parts of the main halo (with $r > 258\,$kpc, such that their tidal radius is larger than r_{250}). Again we find an offset of about a factor of 2 in the mean substructure abundance between field halos and genuine subhalos.

We conclude that the (sub-)substructure abundance in subhalos is *not*, in general, a scaled version of that in main halos. Rather, the self-similar expectation provides an upper limit on the abundance of these second generation substructures; less (sub-)substructure is typically found. This reflects the fact that the substructure abundance of a subhalo is not only diminished by tidal truncation once it falls into a larger structure; in addition, its retained substructures continue to lose mass to the main subhalo through tidal effects and, in strong contrast to the situation for main halos, they are not continually replenished by infall of new subhalos from the field. The substructure deficit in subhalos when compared to main halos *at the same mean overdensity* is expected to grow with time as they orbit within their main halos. It will therefore be more marked in subhalos in the inner halo, which are typically "older".

Our results thus caution strongly against the assumption that subhalos typically have mass fractions in substructure similar to the main halo (as suggested by, e.g., Shaw et al., 2007; Kuhlen et al., 2008).

5 INTERNAL STRUCTURE OF SUBHALOS

In this section we study the structural properties of subhalos, and we compare them to the properties of similar mass isolated halos. We analyze how the density profiles of individual subhalos converge as numerical resolution is increased, and we measure the concentration of subhalos as a function of mass, circular velocity and radial distance. We then compare with the corresponding relations for field halos.

5.1 Density profiles for subhalos

The internal density structure of nonlinear dark matter halos is one of the most important predictions obtained from numerical simulations of the CDM paradigm. The density profile directly affects the rotation curves of galaxies, the

gravitational lensing properties of dark matter halos, and the X-ray luminosity and SZ-signal of galaxy groups and clusters. The density profile of subhalos also determines the kinematics of the stars in satellite galaxies, which are observationally accessible for the dwarf spheroidals around the Milky Way (e.g. Stoehr et al., 2002; Strigari et al., 2007a). Furthermore, the inner density profiles of halos and subhalos are critical for estimating the luminosity in dark matter annihilation radiation, in case such a decay channel exists.

About a decade ago, Navarro et al. (1996, 1997) were able to show that the spherically averaged density profiles of dark matter halos have an approximately universal shape that is well described by a simple fitting formula

$$\rho(r) = \frac{\delta_c\,\rho_{\rm crit}}{(r/r_s)(r/r_s+1)^2} \qquad (13)$$

that has become known as the NFW-profile. In this double power law, the local logarithmic slope gradually changes from a value of -3 in the outer parts to an asymptotic slope of -1 in the inner parts. The spatial scale r_s of this transition is treated as a fitting parameter and is often parameterized in terms of the concentration $c = r_{200}/r_s$ of the halo, which is, in fact, simply a reparameterization of δ_c, the characteristic overdensity relative to the critical density: $\delta_c = (200/3)\,c^3/[\ln(1+c) - c/(1+c)]$. NFW showed the concentration to depend systematically on halo mass, a finding that can be interpreted as reflecting the density of the universe at the time of halo formation. A number of analytic fitting functions for this dependence have been proposed in the literature (Navarro et al., 1997; Bullock et al., 2001; Eke et al., 2001), but only recent large-volume simulations have been able to calibrate it reliably for rare objects like massive galaxy clusters (Neto et al., 2007; Gao et al., 2007).

Ever since the discovery of the NFW profile, the structure of the inner cusp has been the subject of much discussion and controversy. As computing power has increased, many groups have reexamined the value of the inner slope using ever bigger and better resolved simulations, but no consensus has yet emerged (Fukushige & Makino, 1997; Moore et al., 1998, 1999b; Ghigna et al., 2000; Jing & Suto, 2000; Fukushige & Makino, 2001; Klypin et al., 2001; Jing & Suto, 2002; Fukushige & Makino, 2003; Power et al., 2003; Navarro et al., 2004; Fukushige et al., 2004; Diemand et al., 2005; Stoehr, 2006; Knollmann et al., 2008).

It has often been claimed that the inner cusps of halos and subhalos may have slopes less than -1, with some studies even proposing an asymptotic slope of -1.5 (Moore et al., 1999b; Fukushige & Makino, 2001). For main halos this proposition has been ruled out in recent years by newer generations of simulations. Nevertheless, the idea that the asymptotic slope is typically steeper than -1 (e.g. ~ -1.2) is still widespread and has been reiterated in recent papers, even though this is clearly inconsistent with, for example, Fig. 4 or the numerical data in Navarro et al. (2004).

With respect to the density profiles of subhalos, the situation is even more unclear. So far few studies have examined this question directly. Stoehr (2006) found that the circular velocity curves of subhalos are best fit by a parabolic function relating $\log V$ to $\log r$, implying that the density profiles become shallower in the centre than NFW. On the other hand, Diemand et al. (2008) recently argued that subhalos have steep cusps with a mean asymptotic slope of -1.2.

We want to emphasize from the outset that the nature of halo and subhalo density profiles, becoming gradually and monotonically shallower towards the centre, makes it easy to arrive at the wrong conclusion for the structure of the inner cusp. Almost all numerical simulations to date have been able to produce demonstrably converged results for the density profile only in regions where the local slope is significantly steeper than -1. They have also all shown that the slope at the innermost measured point is significantly shallower than at radii a factor of a few further out. Thus, although no slope as shallow as -1 has been found, there is also no convincing evidence that the values measured are close to the asymptotic value, if one exists. Most claims of steep inner cusp slopes are simply based on the assertion that the slope measured at the innermost resolved point continues all the way to the centre.

Navarro et al. (2004) argued that the local logarithmic slope of halo profiles changes smoothly with radius and is poorly fit by models like those of NFW or Moore that tend to an asymptotic value on small scales. They showed that in their simulation data the radial change of the local logarithmic slope can be well described by a power-law in radius, of the form

$$\frac{{\rm d}\log\rho}{{\rm d}\log r} = -2\left(\frac{r}{r_{-2}}\right)^{\alpha}, \qquad (14)$$

which corresponds to a density profile

$$\rho(r) = \rho_{-2}\,\exp\left(-\frac{2}{\alpha}\left[\left(\frac{r}{r_{-2}}\right)^{\alpha} - 1\right]\right). \qquad (15)$$

Here ρ_{-2} and r_{-2} are the density and radius at the point where the local slope is -2. This profile was first used by Einasto (1965) to describe the stellar halo of the Milky Way, so we refer to it as the Einasto profile. The introduction of a shape parameter, α may be expected, of course, to provide improved fits, but we note that fixing $\alpha \sim 0.16$ gives a two-parameter function which still fits mean halo profiles much better than the NFW form over a wide range of halo masses (i.e. with maximum residuals of a few percent rather than 10 percent, Gao et al., 2007). Further evidence for a profile where local slope changes gradually has been presented by Stoehr et al. (2003); Stoehr (2006); Graham et al. (2006). For reference, we note that the enclosed mass for the Einasto profile is

$$M(r) = \frac{4\pi r_{-2}^3\rho_{-2}}{\alpha}\,\exp\left(\frac{3\ln\alpha + 2 - \ln 8}{\alpha}\right)\,\gamma\left[\frac{3}{\alpha}, \frac{2}{\alpha}\left(\frac{r}{r_{-2}}\right)^{\alpha}\right] \qquad (16)$$

where $\gamma(a,x)$ is the lower incomplete gamma function. For a value of $\alpha = 0.18$ the radius where the maximum circular velocity peaks is given by $r_{\rm max} = 2.189\,r_{-2}$, and the maximum circular velocity is related to the parameters of the profile by $V_{\rm max}^2 = 11.19\,G r_{-2}^2\,\rho_{-2}$.

No published simulation to date has had enough dynamic range to measure the logarithmic slope of the density profile in the region where the Einasto model would predict it to be shallower than -1, so only indirect arguments could be advanced for this behaviour (Navarro et al., 2004). This situation has changed with the Aquarius Project, as can be seen from Fig. 4, and in Navarro et al. (2008) we provide a detailed analysis of this question. In the following, we focus on the density profiles of dark matter *subhalos*, where the available particle number is, of course, much smaller.

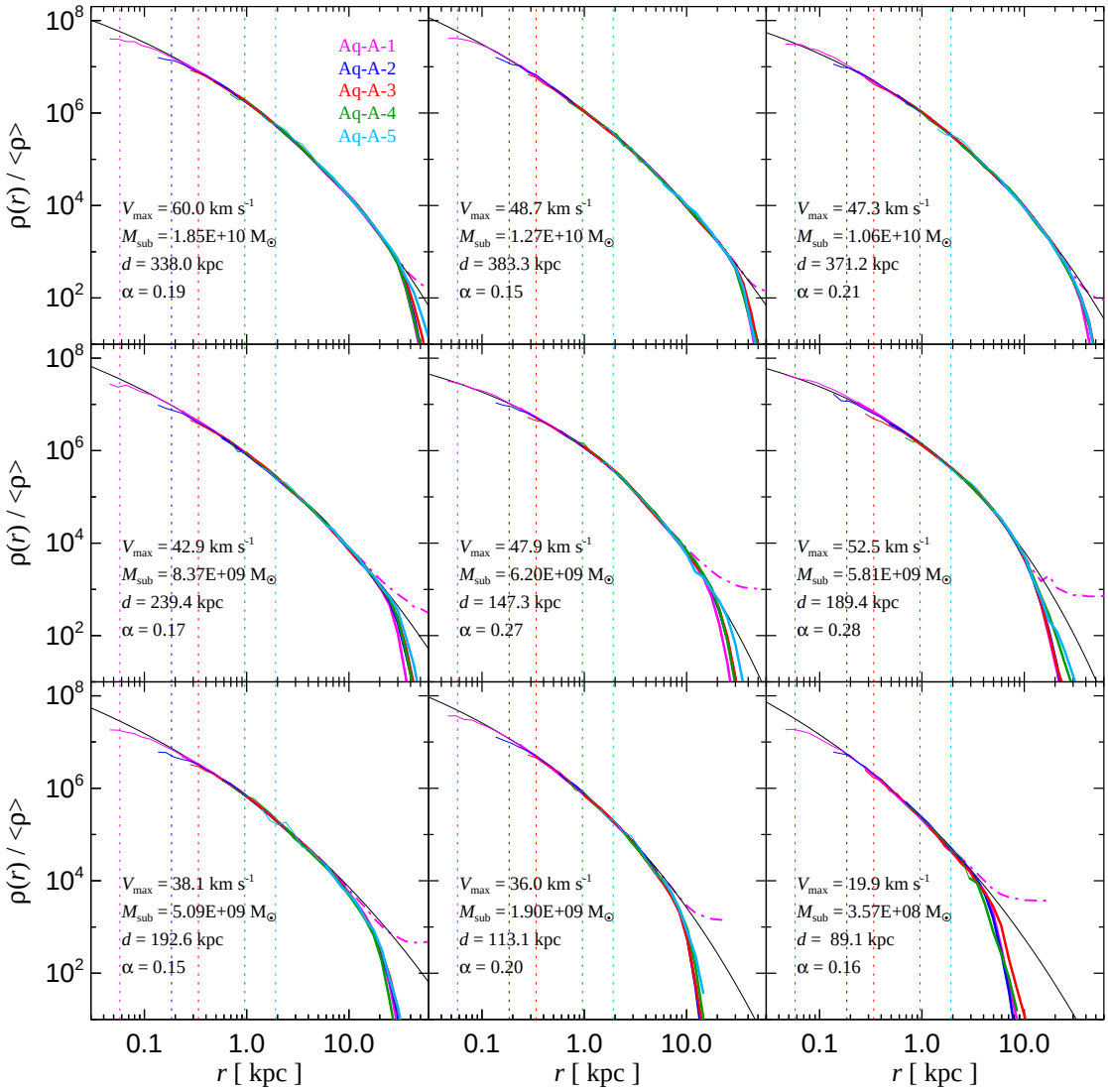

Figure 22. Subhalo density profiles for nine different subhalos in the Aq-A halo, simulated with varying resolution. The profiles show the bound mass only and are drawn with thick lines for the radial range where convergence is expected, based on the criterion of Power et al. (2003). They are continued with thin lines down to the scale $2\,\epsilon$. Vertical dashed lines mark the radii where the force law becomes Newtonian ($2.8\,\epsilon$). The dot-dashed purple line in each panel is the density profile of all the mass around the subhalo's centre (i.e. including unbound mass). The thin black line shows a fit with the Einasto profile. The labels in each panel give the maximum circular velocity, mass, and distance d to halo centre for each subhalo. α is the shape parameter of the Einasto profile, which we here allowed to vary freely in our fits.

Our best resolved subhalos in the Aq-A-1 simulation contain more than 10 million particles, allowing a relatively precise characterization of their density profiles. Until recently, such particle numbers represented the state-of-the-art for simulations of *main* halos.

In Figure 22, we show spherically averaged density profiles for 9 subhalos within the Aq-A halo. For each we compare up to 5 different resolutions, covering a factor of ~ 1835 in particle mass. The density profiles line up quite well outside their individual resolution limits, as predicted by the convergence criterion of Power et al. (2003) in the form given in equation (3). Individual profiles in the panels are plotted as thick solid lines at radii where convergence is expected according to this criterion, but they are extended inwards as thin lines to twice the gravitational softening length (the gravitational force is exactly Newtonian outside the radii marked by vertical dashed lines). These density profiles are based on particles that are gravitationally bound to the subhalos, but for comparison we also show a profile for each subhalo that includes all the mass (i.e. including unbound particles; thick dashed lines). It is clear that the background density dominates beyond the 'edge' of each subhalo. It is therefore important that this region is excluded when fitting analytic model density profiles to the subhalos.

In making such fits, we restrict ourselves to the radial range between the convergence radius (equation 3) and the largest radius where the density of bound mass exceeds 80% of the total mass density. The density profiles themselves are

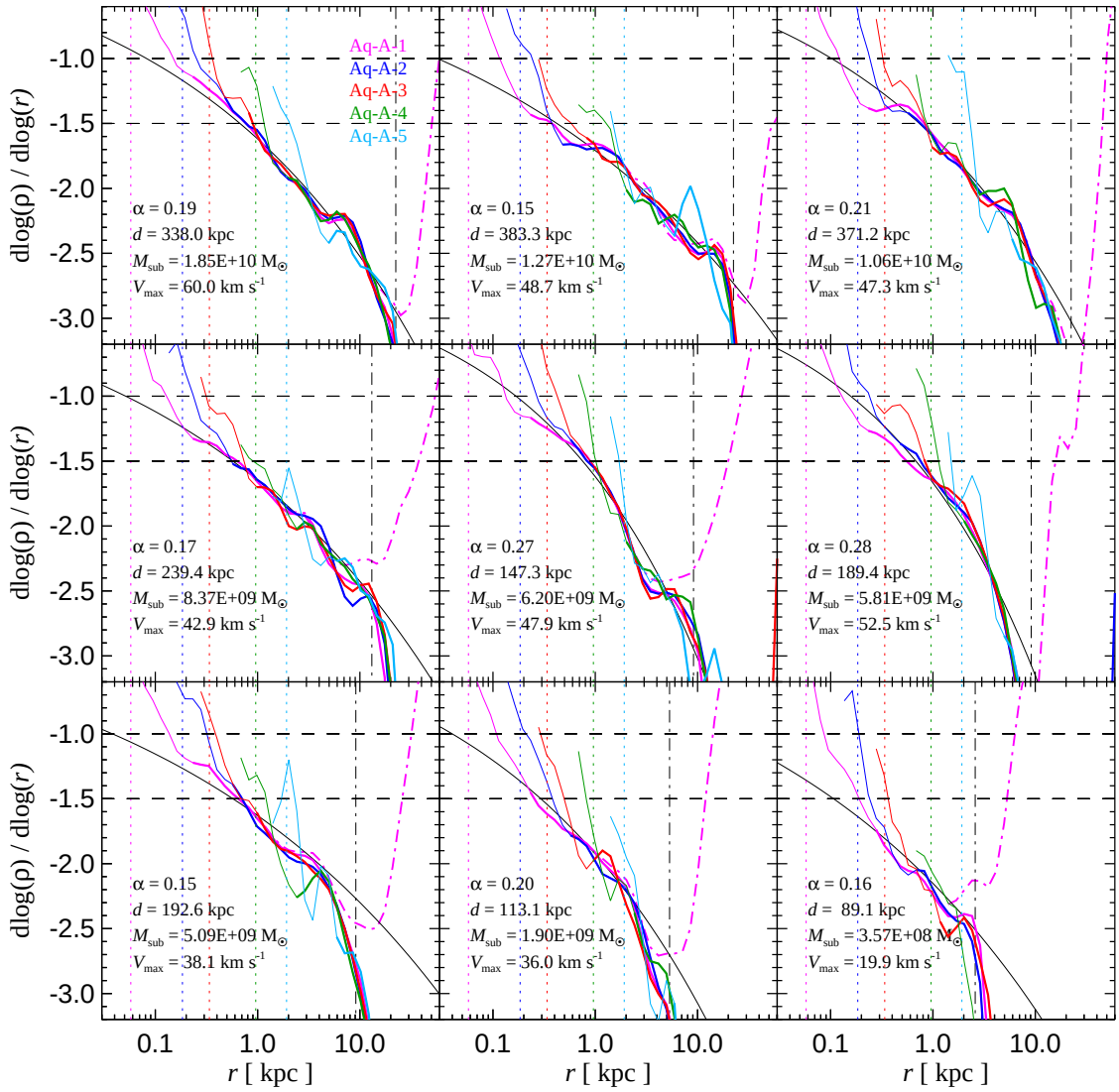

Figure 23. Local logarithmic slope (obtained by numerical differentiation) of the measured density profile for 9 different subhalos, at varying numerical resolution. As in Figure 22, the thick line style is used in regions where numerical convergence is expected. The thin solid line shows a fit with the Einasto profile. Slopes of -1.5 (corresponding to the Moore profile) and of -1.0 (the NFW profile) are marked with horizontal dashed lines.

measured in a set of radial shells spaced equally in $\log r$. To define the best fit, we minimize the sum of the squared differences in the log between measurement and model, i.e. we characterize the goodness of fit by a quantity

$$Q^2 = \frac{1}{N_{\rm bins}} \sum_i [\ln \rho_i - \ln \rho^{\rm model}(r_i)]^2, \qquad (17)$$

where the sum extends over all bins i. We then minimize Q with respect to the parameters of the model profile. We have included such fits as thin solid lines in Figure 22, based on the Einasto profile, allowing the third parameter α to vary as well. The resulting values of α and the maximum circular velocities of the subhalos, as well as their mass and distance to the main halo's centre are shown as labels in the individual panels.

It is clear from Figure 22 that the Einasto profile provides a good description of subhalo radial density profiles, but due to the large dynamic range on the vertical axis combined with the narrow radial range over which the density profile can be fit, it is not clear in this representation whether the Einasto fit is significantly better than fits with other analytic functions, like the NFW or Moore profiles.

Further insight can be obtained by studying the local logarithmic slopes of the subhalo density profiles as a function of radius, which we show in Figure 23, obtained by finite differencing of the measured density profiles. Again, we compare the differing resolutions available for Aq-A, and plot the results as thick lines for radii where we expect convergence according to Power et al. (2003), continuing them with thin lines towards smaller scales. The convergence criterion appears to work quite well and in most cases accurately delineates a limit beyond which the profiles suddenly start to become significantly flatter. At larger radii, the local slopes change continuously and smoothly with radius.

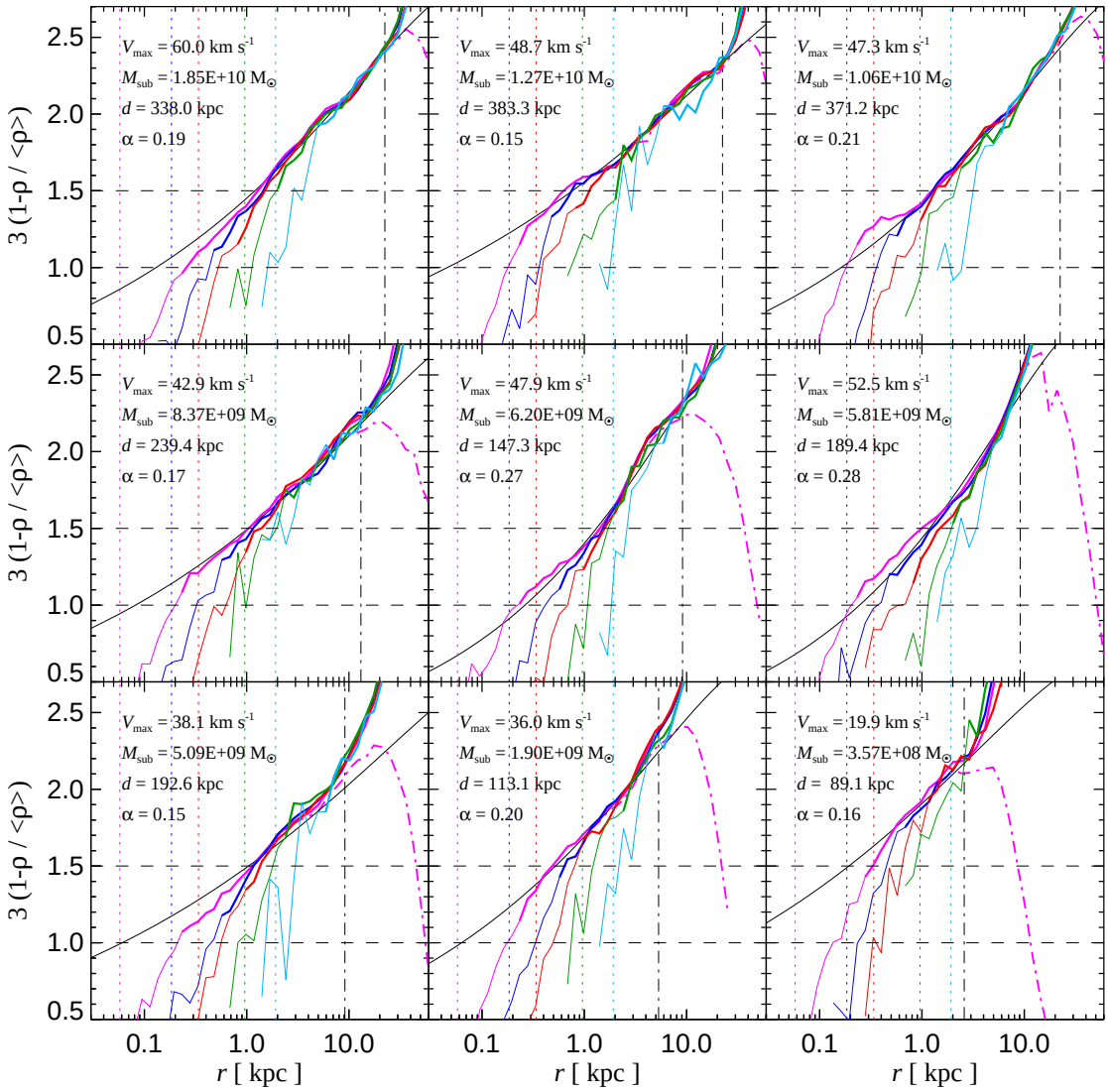

Figure 24. The maximum possible inner asymptotic slope of the density profiles of 9 subhalos in the Aq-A-1 simulation. The plot uses the same linestyles as in Fig. 23. Rather than the local slope of the density profile, this plot shows the most negative slope that is consistent both with the locally enclosed mass, and the local spherically averaged density.

For several subhalos, we have direct evidence that for the local slope is significantly shallower than -1.5 in the innermost converged bin, thereby ruling out the Moore profile for at least some dark matter subhalos. In one case, we find convergence to a slope which is clearly shallower than -1.2. As for main halos, extrapolation of the shape of these curves to smaller radii suggests that profiles that will become significantly shallower before reaching an asymptotic inner slope, if one exists. From these results it seems very unlikely that typical dark matter subhalos could have power law cusps with slopes as steep as -1.2, as recently suggested by Diemand et al. (2008).

Another way to arrive at a similar conclusion is not to consider the numerically differentiated density profile, but rather the maximum asymptotic inner slope

$$\beta(r) = 3[1 - \rho(r)/\overline{\rho}(r)] \qquad (18)$$

that can be supported by the enclosed mass at a certain radius. This quantity was introduced by Navarro et al. (2004). It requires converged values for both the local density and the enclosed mass at each radius r. This is a more stringent convergence requirement than asking that the density alone be converged. Nevertheless, it can provide a powerful lower limit on the profile slope in the inner regions; there cannot possibly be a cusp steeper than $\rho \propto r^{-\beta}$ since there is simply not enough mass enclosed to support it. In Figure 24, we show $\beta(r)$ as a function of radius for the same subhalos as before, using the same approach to mark the Power et al. (2003) convergence radius. We see that this convergence criterion is not conservative enough in some of cases, where the enclosed mass is not fully converged for the last bin. The Power et al. (2003) criterion was actually designed for this quantity, but it has only been tested for main halos, and it is not surprising that we find subhalos to be somewhat more demanding. Nevertheless, this figure reinforces our earlier conclusion. For most of the subhalos, a central

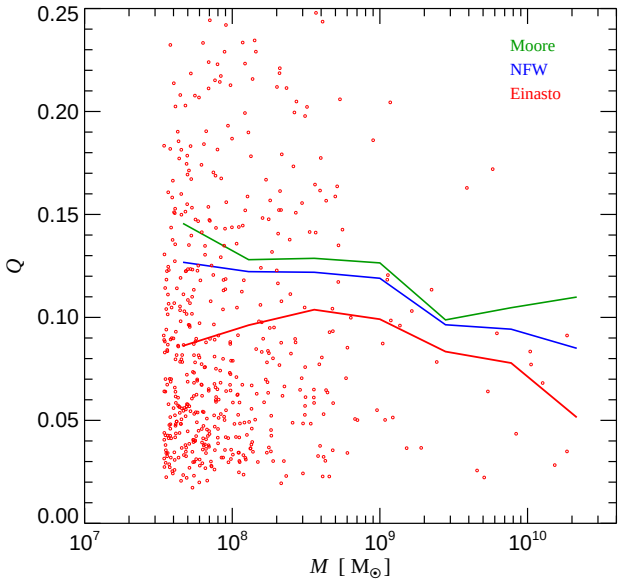

Figure 25. Quality of fits to subhalo density profiles, based on three different two-parameter models, an NFW profile, a Moore profile, and an Einasto profile with $\alpha = 0.18$. The circles show a measure for the mean deviation per bin, Q, for 526 subhalos in the main halo of the Aq-A-1 simulation. The subhalos considered contain between 20,000 and nearly $\sim$ 10 million particles. The lines in different colours show averages in logarithmic mass bins for each of the three profiles.

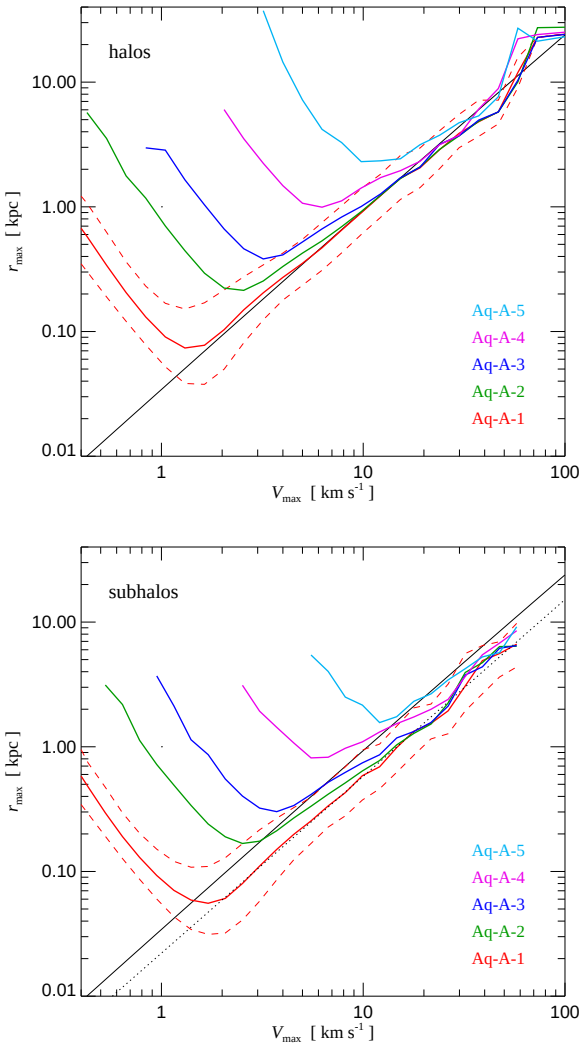

Figure 26. Relation between $r_{\rm max}$ and $V_{\rm max}$ for main halos (top) and subhalos (bottom) in the Aq-A series of simulations. We compare results for simulations of different resolution for this halo, and we use solid lines to mark the mean of $\log r_{\rm max}$ in each bin. The dashed red lines enclose 68% of the distribution for the Aq-A-1 simulation. The solid line is an extrapolation to smaller mass of the result of Neto et al. (2007) for the halos of the Millennium simulation, while the dotted power law in the lower panel is a fit to our results for subhalos, lying a factor 0.62 lower.

dark matter cusp as steep as the Moore profile can be safely excluded, and in a few cases, the limit is shallower than ~ -1.3. Again, the shape of $\beta(r)$ suggests that limits are likely to tighten considerably once still smaller scales can be resolved.

Finally, we would like to answer objectively the question whether the Einasto model fits subhalo profiles better than the NFW or Moore models; in other words, whether it produces smaller residuals overall. To test this question, we fix α for the Einasto profile at $\alpha = 0.18$ so that there are only two free parameters left, as in the NFW and Moore profiles. (These are a characteristic overdensity and a radial scale.) Our results are insensitive to varying α in the range $\sim 0.16 - 0.20$. We estimate best fits for 526 subhalo profiles (considering all subhalos in Aq-A-1 with more than 20,000 particles) by minimizing the quantity Q defined by equation (17) over the radial range between the Power convergence radius and an outer radius defined as above. In Figure 25 we show the results. We plot the mean residual per bin with symbols giving results for the Einasto profile to illustrate the typical scatter. The solid coloured lines are means for the three different profile shapes, calculated for logarithmic bins of subhalo mass. We see that the Einasto profile consistently produces the lowest residuals, followed by the NFW profile, while the Moore profile is consistently the worst. The relatively small difference in the quality of the fit between the NFW and Moore profiles is due to the fact that the resolution limitations for the subhalos restrict the fits to comparatively large radii where the two still have quite similar shape. There appears to be no systematic trend with subhalo mass.

We conclude that the density profiles of subhalos show similar behaviour to those of main halos; the local logarithmic slope becomes gradually shallower with decreasing radius. There is no evidence that a fixed asymptotic power law has been reached at the innermost converged points. Inner cusps as steep as the Moore profile are excluded for most objects, and for some objects we can already exclude logarithmic slopes as steep as -1.3.

5.2 The concentration of subhalos

Because the density profiles of dark matter halos are not pure power laws it is possible to assign them a characteristic density or "concentration". Perhaps the simplest such

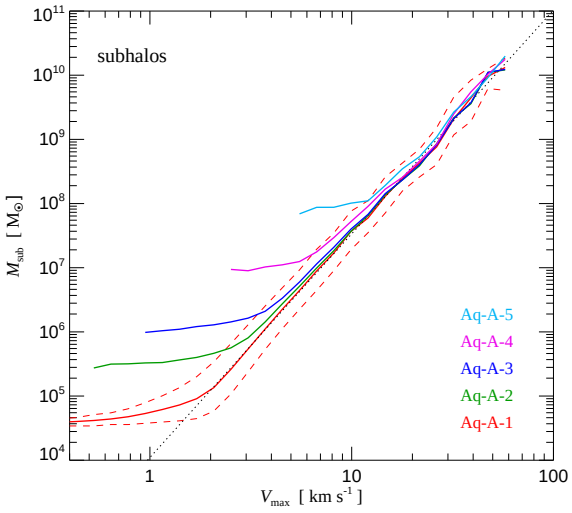

Figure 27. Mean relation between subhalo mass as assigned by SUBFIND and maximum halo circular velocity. The dashed red lines enclose 68% of the distribution around the mean (calculated as an average of $\log M_{\rm sub}$) for the Aq-A-1 simulation. The dotted line is a power law fit, $M_{\rm sub} \simeq 3.37 \times 10^7\,(V_{\rm max}/10\,{\rm km\,s^{-1}})^{3.49}$, to the results of Aq-A-1.

measure is the overdensity (relative to critical) within the radius where the circular velocity curve peaks (see equation 6). In many studies it has been found that halos of a given mass exhibit a well-defined characteristic concentration (Navarro et al., 1997; Eke et al., 2001; Bullock et al., 2001; Neto et al., 2007; Gao et al., 2007), or in other words, that the radius $r_{\rm max}$ at which the circular velocity peaks is tightly correlated with the maximum circular velocity $V_{\rm max}$. Recently, Neto et al. (2007) have given an accurate fit to this relation for halos with masses between about 10^{12} and $10^{15}{\rm M}_\odot$, based on the good statistics provided by the Millennium Simulation.

In the top panel of Figure 26, we show the relationship between $r_{\rm max}$ and $V_{\rm max}$ as measured for main halos in our Aq-A simulation. These are halos that are outside of the main Milky-Way sized halo, but are still contained in the high-resolution region. We make sure to include only halos that are free of any contamination by boundary particles. Comparing the various resolutions available for the 'A' halo, it can be seen that the correlation can be trusted down to about $V_{\rm max} \sim 1.5\,{\rm km\,s^{-1}}$ for our highest resolution calculation, the Aq-A-1 run. Remarkably, we find that the power-law relation of Neto et al. (2007) describes our measurements very accurately, despite the fact that this is an extrapolation by several orders of magnitude into a regime which was previously unconstrained by numerical data.

The bottom panel of Figure 26 shows the equivalent measurements for subhalos that are contained within r_{50} of the main halo. Clearly, these subhalos are typically more concentrated than halos of the same circular velocity in the field, as first found by Ghigna et al. (1998). At equal $V_{\rm max}$, the $r_{\rm max}$ values of subhalos are on average 62% of those of field halos, corresponding to a 2.6 times higher characteristic density. This can be understood as a result of tidal mass loss. As Peñarrubia et al. (2008) show, stripping reduces both $V_{\rm max}$ and $r_{\rm max}$, but the reduction in $r_{\rm max}$ is larger, so that the concentration increases (see also Hayashi et al., 2003; Kazantzidis et al., 2004; Bullock & Johnston, 2005). We note that this effect also increases the characteristic density and the dark matter annihilation luminosity of subhalos relative to halos in the field when they are compared at *equal mass*, contrary to the arguments of Strigari et al. (2007b).

The subhalo masses $M_{\rm sub}$ are tightly correlated with $V_{\rm max}$ as well, as shown in Figure 27. However, the slope of this relation, $M_{\rm sub} \propto V_{\rm max}^{3.5}$, is somewhat steeper than expected for a self-similar scaling of subhalo structure with size. This is again a consequence of tidal mass loss, which affects the mass of a subhalo more than its maximum circular velocity.

Another interesting quantity to consider is the mean characteristic density contrast $\delta_V = V_{\rm max}^2/(H_0 r_{\rm max})^2$ of subhalos. In Figure 28, we show the dependence of this measure of concentration on circular velocity and subhalo mass. Clearly, the concentration increases strongly with decreasing subhalo mass. Interestingly, this trend is equally strong for subhalo samples at different radii, but the absolute values of the concentrations are larger at smaller radii. This is illustrated in Fig. 28 which compares results for the inner halo ($r < 50\,{\rm kpc}$) and for a shell at large radii ($r > 300\,{\rm kpc}$) with results for the halo as a whole.

This radial trend is more directly displayed in Figure 29, where we show the mean characteristic density contrast as a function of radius for samples selected above different lower cut-offs in circular velocity. In general, subhalo concentrations rise towards halo centers, as found by Diemand et al. (2007b, 2008). For comparison, we also show results for Via Lactea II, as recently published by Diemand et al. (2008) where a cut-off of $5\,{\rm km\,s^{-1}}$ was used. Interestingly, our subhalos are substantially more concentrated than those in Via Lactea II for the same lower cut-off. The Via Lactea II subhalos are actually slightly less concentrated than our subhalos selected above $10\,{\rm km\,s^{-1}}$. The origin of this difference is unclear, but it may be related to the discrepancy in the abundance of subhalos that we discussed earlier in Section 3.

6 SUMMARY

In this paper, we have presented first results from the Aquarius Project, a Virgo Consortium[§] programme to carry out high-resolution dark matter simulations of Milky-Way-sized halos in the ΛCDM cosmology. This project seeks clues to the formation of galaxies and to the nature of the dark matter by designing strategies for exploring the formation of our Galaxy and its luminous and dark satellites, for searching for signals from dark matter annihilation, and for designing experiments for the direct detection of dark matter.

In our approach, we pay great attention to validating our numerical results to careful convergence studies. In addition, we explore possible uncertainties in predictions for the Milky Way resulting from the scatter in properties between otherwise similar halos. Thus, we simulate not just one realization at ultra high resolution, but rather a sample of (currently) 6 different halos. Our ambition is to redefine

[§] The Virgo Consortium is an international collaboration of astronomers working on supercomputer simulations of cosmic structure formation, see http://www.virgo.dur.ac.uk

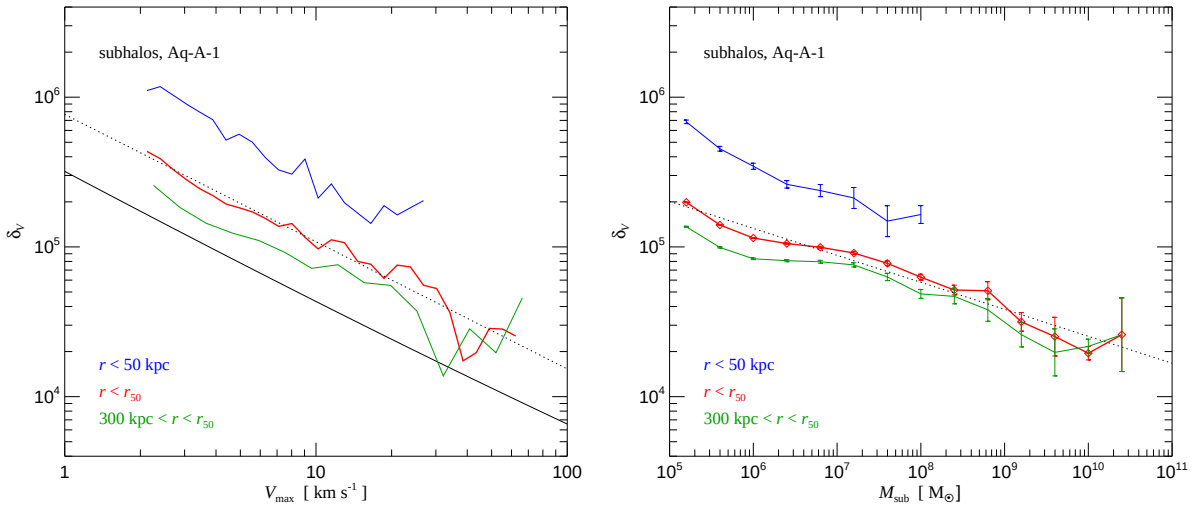

Figure 28. Subhalo characteristic density (which is a measure of concentration) as a function of maximum circular velocity (left panel) and subhalo mass (right panel). We show results for all halos in the r_{50} radius, as well as separately for the inner halo within 50 kpc, and for an outer shell between 300 kpc and r_{50}. The solid line in the left panel gives an extrapolation of the result which Neto et al. (2007) quote for halos in the Millennium simulation, while the dotted power law lies a factor 2.6 higher and fits our results for the subhalos within r_{50}. The dotted line in the right panel, $\delta_V \simeq 5.80 \times 10^8\,(M_{\rm sub}/10^8\,{\rm M}_\odot)^{-0.18}$, is a fit to our results for all subhalos within r_{50}.

the state-of-the-art in this field with respect to the accuracy of the cosmological N-body simulations, and the rigour with which quantitative statements about halo structure can be made.

Our new simulation code GADGET-3, developed specifically for the Aquarius Project, is a highly efficient, massively parallel N-body code. It offers much better scalability to large numbers of compute cores and a higher basic speed than its parent code GADGET-2 (Springel, 2005). It is able to cope efficiently with the tight coupling of around 1.5 billion particles in a single nonlinear object, split up across 1024 CPUs. Some of our simulations at resolution level 2 were run on an even larger number of compute cores, using up to 4096 cores of a Bluegene/P computer. Here we used a novel feature in GADGET-3 that can exploit additional compute cores in shared-memory nodes by means of threads (based on the POSIX pthreads library) yielding a mix of distributed and shared memory parallelism. The ability to simulate this high degree of clustering and nonlinearity on massively parallel architectures is a prerequisite for exploiting the power of upcoming petaflop computers for the next generation of high-precision simulations of cosmological structure formation.

The results presented above demonstrate that we have created a remarkably accurate set of simulations, reaching very good convergence for the dark matter density profile and the substructure mass function over the maximum range that could be expected. Even the location, mass and internal structure of individual large dark matter subhalos reproduce well between simulations of differing resolution, a level of convergence which exceeds anything previously reported in the literature.

The abundance of dark matter subhalos is remarkably uniform across our halo sample when normalized to parent halo mass, and when considering subhalos sufficiently small that fluctuations due to counting statistics are unimportant. The differential subhalo mass function is tilted to a slope slightly shallower than the critical value -2, so that, even when extrapolated to arbitrarily small masses, the total mass fraction in substructures remains small, less than 3% within 100 kpc of halo centre, and less than 20% within $r_{50} \sim 400$ kpc. Adopting the logarithmically divergent slope -2 (which our results appear to exclude) does not increase these mass fractions by more than a factor of 2 or 3 for lower

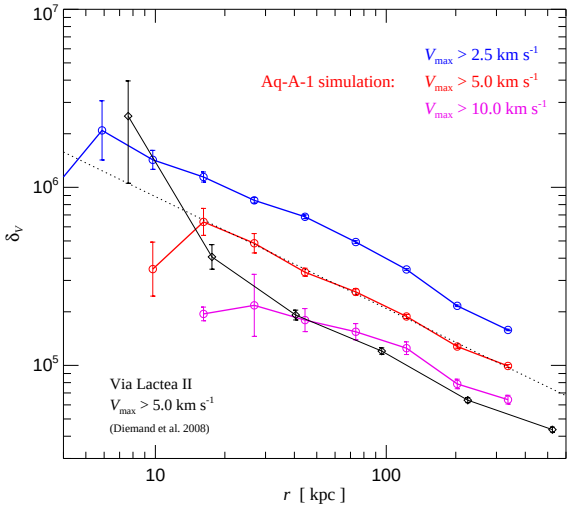

Figure 29. Subhalo concentration as a function of radius, for subhalos with maximum circular velocity larger than 2.5, 5, or 10 km s^{-1}. The dotted line is a fit to our result for the 5 km s^{-1} sample, which yields $\delta_V \simeq 3.77 \times 10^6\,(r/{\rm kpc})^{-0.63}$. For comparison, we have also included the result quoted recently by Diemand et al. (2008) for the Via Lactea II simulation, which selected subhalos with $V_{\rm max} > 5\,{\rm km\,s^{-1}}$. Clearly, our subhalos are more concentrated than theirs at the same circular velocity.

mass limits in the range 10^{-6} to $10^{-12}, \mathrm{M}_{\odot}$, which plausibly correspond to the thermal free-streaming limit if the dark matter is the lightest sypersymmetric particle. The inner halo is dominated by a smoothly distributed dark matter component, not by substructure.

Independent of their present mass, substructures have a *strong* preference to be found in the outer regions of halos. For example, we estimate that at most a fraction of 10^{-3} of the dark matter at the Solar circle is in bound subclumps. The rest is smoothly distributed. Note, however, that this smooth component is expected to have a rich structure in velocity space, being composed of a large number (perhaps 10^5 or more) of cold streams (Helmi et al., 2003; Vogelsberger et al., 2008).

Contrary to previous claims, we find that substructure in subhalos is not a scaled-down version of substructure in main halos. Subhalos typically have less substructure than main halos. This is due to two causes. Tidal stripping removes the outer substructure-rich parts of halos when they fall into a larger system and become subhalos. In addition, as the retained substructure ages it decreases in mass and number and is not replaced by the infall of new objects. As a result, the substructure mass fraction in subhalos is often much smaller than in main halos, particularly for subhalos in the inner regions which are the most heavily stripped and also, typically, the "oldest".

We have presented the first detailed convergence study of the shape of subhalo density profiles to be based on simulation sets where the *same* subhalo can be identified in simulations of differing mass resolution. We find that the inner regions of subhalos, well inside their tidal truncation radii, can be well fit by NFW or Einasto profiles. Einasto fits are typically preferred, even when the shape parameter α is fixed to a standard value, e.g., $\alpha = 0.18$. We have also studied how the local logarithmic slope of the density profile varies with radius, finding profiles to become gradually shallower towards the centre with no sign of approaching an asymptotic power-law behaviour. This is very similar to the behaviour of the central cusp in isolated dark matter halos (Navarro et al., 2004). (We will address main halo cusps using the Aquarius simulations in a forthcoming paper, Navarro et al., 2008). We find many subhalos for which the slope at the innermost converged point is substantially shallower than -1.5, and a few where it is shallower than -1.2. The Moore profile appears firmly excluded as a description of the inner regions of subhalos. It should not be used when modelling the cold dark matter annihilation signal, as in a number of recent papers (e.g. Baltz et al., 2008).

The concentration of subhalos is higher than that of halos of the same circular velocity or of the same mass in the field. This can be understood as a consequence of tidal truncation and mass loss (Kazantzidis et al., 2004; Bullock & Johnston, 2005; Peñarrubia et al., 2008) which lead to a larger reduction of $V_{\rm max}$ than of $r_{\rm max}$. Interestingly, we find that the relationship between $r_{\rm max}$ and $V_{\rm max}$ for *field* halos is very well fit by the fitting function given by Neto et al. (2007) for the Millennium simulation, even though this involves an extrapolation over many orders of magnitude towards lower mass. At the same maximum circular velocity, we find that the $r_{\rm max}$ values of subhalos are, on average, only 62% of those of field halos.

We note that our results disagree with those of the recent Via Lactea I and II simulations (Diemand et al., 2007a; Madau et al., 2008; Diemand et al., 2008; Kuhlen et al., 2008) on several important points. We find substantially more substructure than reported for the Via Lactea simulations, and the discrepancy with Via Lactea I is larger than the expected halo-to-halo scatter, based on our own simulation set. Our subhalos are also more concentrated than those found in the Via Lactea II simulation. We also differ in our conclusions about the amount of (sub-)substructure in subhalos, which we demonstrate to be less than predicted by the hypothesis that subhalos are tidally truncated, but otherwise scaled-down versions of field halos. Finally, we disagree with the claim of Diemand et al. (2008) that subhalos have central power-law cusps with a mean slope of -1.2.

In future work, we will analyze the detailed formation history of the 'Aquarius' halos and the evolution of their substructure. We will also build a new generation of semi-analytic models to follow the evolution of the baryonic component, and we will compare these with full hydrodynamical simulations of these same halos that we have already begun to carry out. This should bring new insights into galaxy formation, and directly address possible small-scale challenges to the ΛCDM theory. The verdict about whether CDM works on such scales is still pending.

ACKNOWLEDGEMENTS

The simulations for the Aquarius Project were carried out at the Leibniz Computing Center, Garching, Germany, at the Computing Centre of the Max-Planck-Society in Garching, at the Institute for Computational Cosmology in Durham, and on the 'STELLA' supercomputer of the LOFAR experiment at the University of Groningen. SW acknowledges the Aspen Center for Physics for providing the perfect atmosphere for final editing of this paper.

REFERENCES

Baltz E. A., Berenji B., Bertone G., et al., 2008, ArXiv e-prints, arXiv:0806.2911
Bardeen J. M., Bond J. R., Kaiser N., Szalay A. S., 1986, ApJ, 304, 15
Bardeen J. M., Steinhardt P. J., Turner M. S., 1983, Phys Rev D, 28, 679
Bergström L., Ullio P., Buckley J. H., 1998, Astroparticle Physics, 9, 137
Binney J., Tremaine S., 1987, Galactic dynamics, Princeton, NJ, Princeton University Press, 1987, 747 p.
Bower R. G., Benson A. J., Malbon R., et al., 2006, MNRAS, 659
Bryan G. L., Norman M. L., 1998, ApJ, 495, 80
Bullock J. S., Johnston K. V., 2005, ApJ, 635, 931
Bullock J. S., Kolatt T. S., Sigad Y., et al., 2001, MNRAS, 321, 559
Calcáneo-Roldán C., Moore B., 2000, Phys Rev D, 62, 12, 123005
Cen R., Miralda-Escude J., Ostriker J. P., Rauch M., 1994, ApJL, 437, L9
Croton D. J., Springel V., White S. D. M., et al., 2006, MNRAS, 365, 11
Davis M., Efstathiou G., Frenk C. S., White S. D. M., 1985, ApJ, 292, 371
de Blok W. J. G., McGaugh S. S., Rubin V. C., 2001, AJ, 122, 2396

De Lucia G., Kauffmann G., Springel V., et al., 2004, MNRAS, 348, 333
Diemand J., Kuhlen M., Madau P., 2007a, ApJ, 657, 262
Diemand J., Kuhlen M., Madau P., 2007b, ApJ, 667, 859
Diemand J., Kuhlen M., Madau P., et al., 2008, ArXiv e-prints, 0805.1244
Diemand J., Moore B., Stadel J., 2004, MNRAS, 352, 535
Diemand J., Zemp M., Moore B., Stadel J., Carollo C. M., 2005, MNRAS, 364, 665
Einasto J., 1965, Trudy Inst. Astroz. Alma-Ata, 51, 87
Eke V. R., Cole S., Frenk C. S., 1996, MNRAS, 282, 263
Eke V. R., Navarro J. F., Steinmetz M., 2001, ApJ, 554, 114
Flores R. A., Primack J. R., 1994, ApJL, 427, L1
Frenk C. S., White S. D. M., Bode P., et al., 1999, ApJ, 525, 554
Frenk C. S., White S. D. M., Davis M., Efstathiou G., 1988, ApJ, 327, 507
Fukushige T., Kawai A., Makino J., 2004, ApJ, 606, 625
Fukushige T., Makino J., 1997, ApJL, 477, L9
Fukushige T., Makino J., 2001, ApJ, 557, 533
Fukushige T., Makino J., 2003, ApJ, 588, 674
Gaitskell R. J., 2004, Annual Review of Nuclear and Particle Science, 54, 315
Gao L., Navarro J. F., Cole S., et al., 2007, ArXiv e-prints, 0711.0746
Gao L., White S. D. M., Jenkins A., Stoehr F., Springel V., 2004, MNRAS, 355, 819
Gelb J. M., Bertschinger E., 1994, ApJ, 436, 467
Ghigna S., Moore B., Governato F., Lake G., Quinn T., Stadel J., 1998, MNRAS, 300, 146
Ghigna S., Moore B., Governato F., Lake G., Quinn T., Stadel J., 2000, ApJ, 544, 616
Graham A. W., Merritt D., Moore B., Diemand J., Terzic B., 2006, AJ, 132, 2701
Green A. M., Hofmann S., Schwarz D. J., 2004, MNRAS, 353, L23
Guth A. H., 1981, Phys Rev D, 23, 347
Hawking S. W., 1982, Physics Letters B, 115, 295
Hayashi E., Navarro J. F., 2006, MNRAS, 373, 1117
Hayashi E., Navarro J. F., Power C., et al., 2004, MNRAS, 355, 794
Hayashi E., Navarro J. F., Taylor J. E., Stadel J., Quinn T., 2003, ApJ, 584, 541
Helmi A., White S. D., Springel V., 2002, Phys Rev D, 66, 6, 063502
Helmi A., White S. D. M., Springel V., 2003, MNRAS, 339, 834
Hernquist L., Katz N., Weinberg D. H., Miralda-Escudé J., 1996, ApJL, 457, L51
Hofmann S., Schwarz D. J., Stöcker H., 2001, Phys Rev D, 64, 8, 083507
Ishiyama T., Fukushige T., Makino J., 2007, ArXiv e-prints, 0708.1987
Jenkins A., Frenk C. S., White S. D. M., et al., 2001, MNRAS, 321, 372
Jing Y. P., Suto Y., 2000, ApJL, 529, L69
Jing Y. P., Suto Y., 2002, ApJ, 574, 538
Kazantzidis S., Mayer L., Mastropietro C., Diemand J., Stadel J., Moore B., 2004, ApJ, 608, 663
Klypin A., Kravtsov A. V., Bullock J. S., Primack J. R., 2001, ApJ, 554, 903
Klypin A., Kravtsov A. V., Valenzuela O., Prada F., 1999, ApJ, 522, 82
Knollmann S. R., Power C., Knebe A., 2008, MNRAS, 385, 545
Komatsu E., Dunkley J., Nolta M. R., et al., 2008, ArXiv e-prints, 0803.0547
Kuhlen M., Diemand J., Madau P., 2008, ArXiv e-prints, 0805.4416
Ludlow A. D., Navarro J. F., Springel V., Jenkins A., Frenk C. S., Helmi A., 2008, ArXiv e-prints, 0801.1127
Madau P., Diemand J., Kuhlen M., 2008, ArXiv e-prints, 0802.2265
McGaugh S. S., de Blok W. J. G., 1998, ApJ, 499, 41
Moore B., 1994, Nature, 370, 629
Moore B., Calcáneo-Roldán C., Stadel J., et al., 2001, Phys Rev D, 64, 6, 063508
Moore B., Ghigna S., Governato F., et al., 1999a, ApJL, 524, L19
Moore B., Governato F., Quinn T., Stadel J., Lake G., 1998, ApJL, 499, L5
Moore B., Quinn T., Governato F., Stadel J., Lake G., 1999b, MNRAS, 310, 1147
Nagai D., Kravtsov A. V., 2005, ApJ, 618, 557
Navarro J. F., Frenk C. S., White S. D. M., 1996, ApJ, 462, 563
Navarro J. F., Frenk C. S., White S. D. M., 1997, ApJ, 490, 493
Navarro J. F., Hayashi E., Power C., et al., 2004, MNRAS, 349, 1039
Navarro J. F., White S. D. M., Frenk C. S., et al., 2008, in preparation
Neto A. F., Gao L., Bett P., et al., 2007, MNRAS, 381, 1450
Peñarrubia J., Navarro J. F., McConnachie A. W., 2008, ApJ, 673, 226
Power C., Navarro J. F., Jenkins A., et al., 2003, MNRAS, 338, 14
Reed D., Governato F., Quinn T., Gardner J., Stadel J., Lake G., 2005, MNRAS, 359, 1537
Seljak U., Zaldarriaga M., 1996, ApJ, 469, 437
Shaw L. D., Weller J., Ostriker J. P., Bode P., 2007, ApJ, 659, 1082
Springel V., 2005, MNRAS, 364, 1105
Springel V., Hernquist L., 2002, MNRAS, 333, 649
Springel V., White S. D. M., Frenk C. S., et al., 2008, Nature, submitted
Springel V., White S. D. M., Jenkins A., et al., 2005, Nature, 435, 629
Springel V., White S. D. M., Tormen G., Kauffmann G., 2001a, MNRAS, 328, 726
Springel V., Yoshida N., White S. D. M., 2001b, New Astronomy, 6, 79
Starobinsky A. A., 1982, Physics Letters B, 117, 175
Stoehr F., 2006, MNRAS, 365, 147
Stoehr F., White S. D. M., Springel V., Tormen G., Yoshida N., 2003, MNRAS, 345, 1313
Stoehr F., White S. D. M., Tormen G., Springel V., 2002, MNRAS, 335, L84
Strigari L. E., Bullock J. S., Kaplinghat M., Diemand J., Kuhlen M., Madau P., 2007a, ApJ, 669, 676
Strigari L. E., Koushiappas S. M., Bullock J. S., Kaplinghat M., 2007b, Phys Rev D, 75, 8, 083526
Tormen G., Diaferio A., Syer D., 1998, MNRAS, 299, 728
Vogelsberger M., White S. D. M., Helmi A., Springel V., 2008, MNRAS, 385, 236
Wambsganss J., Bode P., Ostriker J. P., 2004, ApJL, 606, L93
Wang J., De Lucia G., Kitzbichler M. G., White S. D. M., 2008, MNRAS, 384, 1301
Warren M. S., Quinn P. J., Salmon J. K., Zurek W. H., 1992, ApJ, 399, 405
White S. D. M., 1996, in Cosmology and Large-Scale Structure, edited by R. Schaefer, J. Silk, M. Spiro, J. Zinn-Justin, Dordrecht: Elsevier, astro-ph/9410043
White S. D. M., Frenk C. S., 1991, ApJ, 379, 52
White S. D. M., Rees M. J., 1978, MNRAS, 183, 341
Zentner A. R., Bullock J. S., 2003, ApJ, 598, 49